



**HAL**  
open science

# Resolved Nuclear Kinematics Link the Formation and Growth of Nuclear Star Clusters with the Evolution of Their Early- and Late-type Hosts

Francesca Pinna, Nadine Neumayer, Anil Seth, Eric Emsellem, Dieu Nguyen, Torsten Böker, Michele Cappellari, Richard Mcdermid, Karina Voggel, C. Jakob Walcher

## ► To cite this version:

Francesca Pinna, Nadine Neumayer, Anil Seth, Eric Emsellem, Dieu Nguyen, et al.. Resolved Nuclear Kinematics Link the Formation and Growth of Nuclear Star Clusters with the Evolution of Their Early- and Late-type Hosts. *The Astrophysical Journal*, 2021, 921 (1), pp.8. 10.3847/1538-4357/ac158f . hal-03416361

**HAL Id: hal-03416361**

**<https://hal.science/hal-03416361>**

Submitted on 9 Dec 2021

**HAL** is a multi-disciplinary open access archive for the deposit and dissemination of scientific research documents, whether they are published or not. The documents may come from teaching and research institutions in France or abroad, or from public or private research centers.

L'archive ouverte pluridisciplinaire **HAL**, est destinée au dépôt et à la diffusion de documents scientifiques de niveau recherche, publiés ou non, émanant des établissements d'enseignement et de recherche français ou étrangers, des laboratoires publics ou privés.



Distributed under a Creative Commons Attribution 4.0 International License



# Resolved Nuclear Kinematics Link the Formation and Growth of Nuclear Star Clusters with the Evolution of Their Early- and Late-type Hosts

Francesca Pinna<sup>1</sup> , Nadine Neumayer<sup>1</sup> , Anil Seth<sup>2</sup> , Eric Emsellem<sup>3</sup> , Dieu D. Nguyen<sup>4</sup> , Torsten Böker<sup>5</sup> , Michele Cappellari<sup>6</sup> , Richard M. McDermid<sup>7</sup> , Karina Voggel<sup>8</sup> , and C. Jakob Walcher<sup>9</sup>

<sup>1</sup>Max Planck Institute for Astronomy, D-69117 Heidelberg, Germany; [pinna@mpia.de](mailto:pinna@mpia.de)

<sup>2</sup>Department of Physics and Astronomy, University of Utah, UT 84112, USA

<sup>3</sup>European Southern Observatory, D-85748 Garching bei Muenchen, Germany

<sup>4</sup>National Astronomical Observatory of Japan (NAOJ), National Institute of Natural Sciences (NINS), 2-21-1 Osawa, Mitaka, Tokyo 181-8588, Japan

<sup>5</sup>European Space Agency/STScI, Baltimore, MD 21218, USA

<sup>6</sup>Department of Physics, University of Oxford, OX1 3RH, UK

<sup>7</sup>Research Centre for Astronomy, Astrophysics, and Astrophotonics, Macquarie University, Sidney, NSW 2109, Australia

<sup>8</sup>Universite de Strasbourg, CNRS, Observatoire astronomique de Strasbourg, UMR 7550, F-67000 Strasbourg, France

<sup>9</sup>Leibniz-Institut für Astrophysik Potsdam (AIP) D-14482 Potsdam, Germany

Received 2021 April 17; revised 2021 July 1; accepted 2021 July 15; published 2021 October 26

## Abstract

We present parsec-scale kinematics of 11 nearby galactic nuclei, derived from adaptive-optics assisted integral-field spectroscopy at (near-infrared) CO band-head wavelengths. We focus our analysis on the balance between ordered rotation and random motions, which can provide insights into the dominant formation mechanism of nuclear star clusters (NSCs). We divide our target sample into late- and early-type galaxies, and discuss the nuclear kinematics of the two subsamples, aiming at probing any link between NSC formation and host galaxy evolution. The results suggest that the dominant formation mechanism of NSCs is indeed affected by the different evolutionary paths of their hosts across the Hubble sequence. More specifically, nuclear regions in late-type galaxies are on average more rotation dominated, and the formation of nuclear stellar structures is potentially linked to the presence of gas funneled to the center. Early-type galaxies, in contrast, tend to display slowly rotating NSCs with lower ellipticity. However, some exceptions suggest that in specific cases, early-type hosts can form NSCs in a way similar to spirals.

*Unified Astronomy Thesaurus concepts:* [Galaxy kinematics \(602\)](#); [Galaxy formation \(595\)](#); [Galaxy evolution \(594\)](#); [Galaxy nuclei \(609\)](#); [Early-type galaxies \(429\)](#); [Late-type galaxies \(907\)](#)

*Supporting material:* figure set

## 1. Introduction

Nuclear star clusters (NSCs) are very compact and bright objects, with average sizes of about 3 pc (see the review by Neumayer et al. 2020). Their sizes, similar to globular clusters (GCs), combined with their higher masses, make them the densest known stellar systems. Observations of NSCs have proven very challenging since their first detection (Redman & Shirley 1937; Babcock 1939; Mayall & Aller 1942). In addition to their small size, they are embedded in the bright central region of their host, and require high spatial resolution to be disentangled as a different morphological component (e.g., Light et al. 1974). While later studies showed that many nearby galaxies of different Hubble types host NSCs (e.g., Caldwell 1983; Kormendy & Djorgovski 1989; van den Bergh 1995; Matthews & Gallagher 1997), only with the resolution of the Hubble Space Telescope (HST) was it possible to find out that NSCs are actually present in most spiral and early-type galaxies (Carollo et al. 1998; Böker et al. 2002; Côté et al. 2006). We now know that most galaxies of all types between  $\sim 10^8$  and  $10^{10} M_{\odot}$  host NSCs, which are also found in a majority of more massive spiral galaxies (Neumayer et al. 2020).

Once nucleation was revealed to be a common phenomenon in all kinds of galaxies, the formation of NSCs assumed a greater importance in the context of galaxy evolution. One possible formation scenario consists of the orbital decay of stellar clusters toward the galactic center, due to dynamical friction, and their subsequent merging. This was first proposed by Tremaine et al. (1975) and later supported by analytical and numerical studies (e.g., Capuzzo-Dolcetta 1993; Oh & Lin 2000; Lotz et al. 2001). On the other hand, in situ star formation after gas infall to the center was proposed as an alternative (e.g., Silk et al. 1987; Mihos & Hernquist 1994; Milosavljević 2004; Bekki 2015). By and large, NSC formation remains still unclear in spite of the following efforts.

Scaling relations between NSCs and the underlying galaxy, such as the NSC-to-galaxy mass relation, have clearly pointed to a tight connection of their formation and growth with the evolution of their host (e.g., Graham & Guzmán 2003; Ferrarese et al. 2006). The nucleation fraction is highest for host stellar masses of about  $10^9 M_{\odot}$ , suggesting that the NSC formation mechanisms are most effective in this mass range (e.g., Sánchez-Janssen et al. 2019). This is true for both early- and late-type galaxies, while the decline in nucleation for larger masses is sharp for ellipticals but not clear for massive late types (Neumayer et al. 2020). On the other hand, more massive galaxies ( $\gtrsim 10^{10} M_{\odot}$ ) seem to host denser nuclear stellar systems (Pechetti et al. 2020). Environmental effects may also play a role for early-type galaxies, which appear to be more



Original content from this work may be used under the terms of the [Creative Commons Attribution 4.0 licence](#). Any further distribution of this work must maintain attribution to the author(s) and the title of the work, journal citation and DOI.

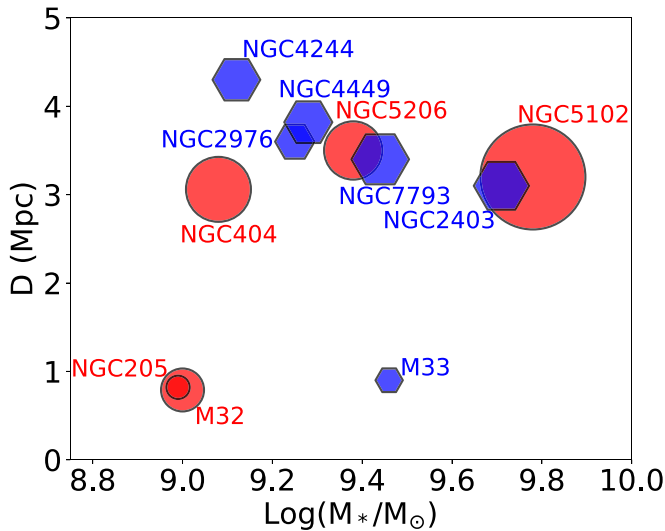


**Figure 1.** Distribution of the galaxy sample in the distance-stellar-mass plane. Red circles and blue hexagons indicate early-type and late-type galaxies, respectively. The names of the host galaxies are indicated close to the individual points. The size of the symbols is proportional to  $R_{e,\text{NSC}}$  according to Table 1.

frequently nucleated toward the central regions of galaxy clusters (e.g., Ferguson & Sandage 1989; Lim et al. 2018).

Since different morphological types of galaxies are related to different evolution histories, it is natural to wonder whether they also form their NSCs in a different way. Stellar populations can give us important insight on this issue. In late-type galaxies, usually characterized by recent star formation, we observe a mix of nuclear stellar populations with the ubiquity of very young stars (e.g., Bothun et al. 1985; Rossa et al. 2006; Seth et al. 2006; Walcher et al. 2006; Kacharov et al. 2018). In early-type galaxies, it is less clear how common young stars are. Their star formation was often quenched earlier, and their NSCs are often younger than their hosts but do not show signs of ongoing star formation (e.g., Paudel et al. 2011; Spengler et al. 2017; Kacharov et al. 2018). Compared to their early-type hosts, they are more metal-rich for host masses above  $10^9 M_\odot$ , but they are often more metal-poor in the low-mass regime (e.g., Neumayer et al. 2020). No similar trend has been observed for late types, but here the picture is complicated by the absence of spectroscopic data in the low-mass regime.

Different observational results have been interpreted as arguments in favor of one or another formation scenario. The spatial distribution and the frequency of GCs in nucleated galaxies, as well as the low metallicity of NSCs of low-mass early types, point to the cluster migration scenario (e.g., Lotz et al. 2001; Capuzzo-Dolcetta & Mastrobuono-Battisti 2009; Lim et al. 2018; Fahrion et al. 2020). On the other hand, the presence of very young populations, extended star formation histories, and gradual chemical enrichment in NSCs hosted by late types, strongly support their in situ formation (e.g., Seth et al. 2006; Walcher et al. 2006; Feldmeier-Krause et al. 2015; Kacharov et al. 2018). In addition, the inflow of molecular gas into the central parsecs from larger-scale structures such as bars, disks, or rings was mapped in late-type spirals and proposed as the driving mechanism for nuclear starbursts (Schinnerer et al. 2003, 2006). However, the properties of NSCs in early- and late-type galaxies are quite heterogeneous, and there is no agreement yet on one dominant formation mechanism. Recent studies point to different origins for the

NSCs in different galaxies, while more than one scenario could have played a role in the central region of one galaxy (e.g., Lyubenova et al. 2013; Guillard et al. 2016; Kacharov et al. 2018).

Stellar kinematics, which contain the footprint of the dynamical history of galactic structures, can provide additional constraints for the origin of NSCs. Kinematic maps provided by integral-field spectroscopy (IFS) have revealed that most NSCs rotate, albeit at different levels (Seth et al. 2008; Seth 2010; Seth et al. 2010; Lyubenova et al. 2013; Nguyen et al. 2018; Fahrion et al. 2019; Lyubenova & Tsatsi 2019). On the one hand, in situ star formation from gas with high levels of angular momentum is often invoked to explain strong NSC rotation. On the other hand, more random motions and complex kinematic structures are usually associated with star-cluster inspiral (e.g., Seth et al. 2008; Seth 2010; Seth et al. 2010; Hartmann et al. 2011; Nguyen et al. 2018). However, recent simulations have supported the idea that observed levels of rotation can be achieved even by star-cluster merging only (Tsatsi et al. 2017; Lyubenova & Tsatsi 2019).

In this paper we provide a kinematic analysis of the nuclear regions of 11 galaxies across the Hubble sequence, and use it to assess whether a specific scenario is likely responsible for NSC formation in early- and late-type galaxies. The paper is organized as follows. In Section 2 we describe the galaxy sample. Section 3 gives the relevant information about the data set. In Section 4 we describe the methods used to perform the kinematic analysis. The results of this are presented in Section 5 and discussed in Section 6. We sum up our conclusions in Section 7. A more detailed description of the individual host galaxies and their nuclear kinematics, as well as a short discussion on the formation of their NSCs, are included in Appendix A.

## 2. The Sample

In this paper, we study the nuclear regions of 11 galaxies with previous NSC detection. The sample was selected to be sufficiently nearby (within a distance of 5 Mpc; see Figure 1), to enable parsec-scale resolution, and to contain early and late Hubble types in roughly equal numbers. Host stellar masses range from 1 to  $6 \times 10^9 M_\odot$ , as illustrated in Figure 1. Additional relevant properties of the individual host galaxies and their NSCs are indicated in Table 1. The photometric properties of the NSCs ( $R_{e,\text{NSC}}$  and  $n_{\text{NSC}}$ , respectively, the effective radius and the Sérsic index) are important for our analysis (see Section 4.5), and we selected literature data in filters as close as possible in wavelength to our near-infrared (NIR) spectroscopic observations.

Hints of past interactions, such as warps, shells, tidal tails, and complex kinematic and morphological structures, are common across the sample (see Appendix A). These galaxies generally contain gas, albeit at different levels of significance. This is true even for the early types, with the exception of M32, which probably has been completely stripped of all gas by past strong interactions. Some early types, such as NGC 404, show extended and complex atomic-gas structures. As expected, our late-type spirals show intense ongoing star formation and some of them show signs of gas inflow toward the center (e.g., galactic fountains in M33 and NGC 2403). Additional details on the individual galaxies are given in Appendix A.

**Table 1**  
Relevant Properties of Our Galaxy Sample and Their NSCs

Galaxy Name	Alternative Name	Hubble Type ( <sup>1</sup> )	$D$ (Mpc)	$M_*$ ( $10^9 M_\odot$ )	$R_{e,\text{NSC}}$ (pc)	$n_{\text{NSC}}$
M 32	NGC 221	E	0.79 ( <sup>2</sup> )	1.00 ( <sup>2</sup> )	4.4 ( <sup>2</sup> )	2.7 ( <sup>2</sup> )
M 33	NGC 598	Scd	0.9 ( <sup>3</sup> )	2.9 ( <sup>6</sup> )	1.8 ( <sup>3</sup> )	3.8 ( <sup>3</sup> )
NGC 205	M 110	E	0.82 ( <sup>2</sup> )	0.97 ( <sup>2</sup> )	1.3 ( <sup>2</sup> )	1.6 ( <sup>2</sup> )
NGC 404	UGC 718	S0	3.06 ( <sup>4</sup> )	1.2 ( <sup>4</sup> )	10.1 ( <sup>4</sup> )	2.6 ( <sup>4</sup> )
NGC 2403	UGC 3918	Scd	3.1 ( <sup>3</sup> )	5.1 ( <sup>7</sup> )	7.3 ( <sup>3</sup> )	2.1 ( <sup>3</sup> )
NGC 2976	UGC 5221	Sc	3.6 ( <sup>3</sup> )	1.8 ( <sup>7</sup> )	3.7 ( <sup>3</sup> )	5.3 ( <sup>3</sup> )
NGC 4244	UGC 7322	Scd	4.3 ( <sup>3</sup> )	1.3 ( <sup>8</sup> )	5.0–5.9 ( <sup>3</sup> )	1.1–2.4 ( <sup>3</sup> )
NGC 4449	UGC 7592	Irr	3.82 ( <sup>5</sup> )	1.9 ( <sup>8</sup> )	5.5 ( <sup>9</sup> )	
NGC 5102	ESO 382-50	S0	3.2 ( <sup>2</sup> )	6.0 ( <sup>2</sup> )	26.3 ( <sup>2</sup> )	0.8–3.1 ( <sup>2</sup> )
NGC 5206	ESO 220-18	S0	3.5 ( <sup>2</sup> )	2.4 ( <sup>2</sup> )	8.1 ( <sup>2</sup> )	0.8–2.3 ( <sup>2</sup> )
NGC 7793	ESO 349-12	Sd	3.4 ( <sup>3</sup> )	2.8 ( <sup>7</sup> )	7.9 ( <sup>3</sup> )	3.3 ( <sup>3</sup> )

**Notes.** Columns from left to right: galaxy name, alternative name, Hubble type, galaxy distance ( $D$ ), galaxy stellar mass ( $M_*$ ), effective (half-light) radius of the NSC ( $R_{e,\text{NSC}}$ ), and Sérsic index of the NSC ( $n_{\text{NSC}}$ ). For  $R_{e,\text{NSC}}$  and  $n_{\text{NSC}}$ , we chose the values obtained from the HST filters with the closest central wavelength to our NIR data, among the ones available in the literature (see table notes). (1) From NASA/IPAC Extragalactic Database. NGC 205 and NGC 5206 are classified as dwarf ellipticals in other references (e.g., Caldwell 1983; Zinnecker & Cannon 1986). (2) Nguyen et al. (2018).  $R_{e,\text{NSC}}$  and  $n_{\text{NSC}}$  were obtained fitting HST images in the following filters: F814W for M 32, NGC 205 and NGC 5206, F547M for NGC 5102. For NGC 5206 and NGC 5102, whose NSCs were fitted with two Sérsic components, we adopted the integrated  $R_{e,\text{NSC}}$ . Since  $n_{\text{NSC}}$  is not available for the integrated NSC, we indicate both indices; (3) Carson et al. (2015).  $R_{e,\text{NSC}}$  and  $n_{\text{NSC}}$  were obtained fitting HST images obtained with the F153M filter. We show, for NGC 4244, the  $R_{e,\text{NSC}}$  and  $n_{\text{NSC}}$  of the two Sérsic components used to fit the NSC. (4) Seth et al. (2010). NGC 404’s total mass was estimated using the bulge-to-total luminosity and the bulge mass (Table 1 in Seth et al. 2010), and assuming a constant mass-to-light ratio. (5) Annibali et al. (2008). (6) McConnachie (2012). (7) de Blok et al. (2008). (8) Sheth et al. (2010). (9) Georgiev & Böker (2014).

### 3. Observations and Data Reduction

In this work we used IFS data in the  $K$  band, corrected by adaptive optics (AO), of the inner  $\sim 3''$  of the 11 galaxies in our sample. We took advantage of facilities in both hemispheres that provide similar capabilities, namely Gemini North in Hawaii, and the Very Large Telescope (VLT) in Chile. Here we provide a summary of the two data sets, and how they were processed prior to the kinematic analysis.

#### 3.1. NIFS Data

We reanalyzed in a consistent way previously published data from the Near-infrared Integral Field Spectrograph (NIFS; McGregor et al. 2003) for M 32 (Seth 2010), NGC 205 (Nguyen et al. 2018), NGC 404 (Seth et al. 2010), and NGC 4244 (Seth et al. 2008). In addition, we present new NIFS data for M 33, NGC 2403, NGC 2976, and NGC 4449. NIFS has a field of view (FOV) of  $3'' \times 3''$  and a spectral range between 0.95 and 2.4  $\mu\text{m}$ . It is mounted on the Gemini North 8 m telescope and offers an AO mode thanks to the ALTAIR (ALTitude conjugate Adaptive optics for the InfraRed) facility (Boccas et al. 2006). Laser-guide-star (LGS) AO was used for all galaxies except M 32, for which a natural guide star (NGS) was used.

Data reduction was performed using pipelines based on the Gemini version 1.9 IRAF packages, as described in Seth et al. (2008, 2010). The final cubes were created from several dithered cubes, which were previously telluric corrected and sky subtracted, using dedicated exposures collected just before or after observing the science object. For the merging of the dithered cubes into the final one, spaxels were rebinned to a size of  $0''.05 \times 0''.05$ . Detailed description of the observations and the data-reduction procedure can be found in Seth et al. (2008, 2010), Seth (2010), and Nguyen et al. (2018).

The point-spread function (PSF) is described, for the previously published data, in the respective papers, cited at the beginning of this subsection. A two-step approach was used to fit the PSF. A first estimate came from images created from the telluric calibrator. Then, a convolution of a high-resolution HST image

with this PSF allowed us to refine the fit, by the comparison of these convolved images with the continuum images from NIFS observations. The best PSF choice was a double component in most cases, an inner Gaussian and an outer Moffat, while it was a simple Gaussian for NGC 4244 (see individual references for the details). We fitted in this work the PSF of M 33, NGC 2403, and NGC 2976, following the same approach but using a double Gaussian, that gave the best fit. The HST images used for the PSF fits were taken with the following two filters: F1042M for M 32 and M 33, and F814W for NGC 205, NGC 404, NGC 2403, NGC 2976, and NGC 4244. Parameters and references of all fits are indicated in Appendix D. We do not have any PSF measurement for NGC 4449. The complexity of its central region made it impossible to derive a PSF for our data cubes from optical images.

With a spectral resolution of  $R \sim 5000$ , NIFS has an approximately Gaussian line-spread function (LSF), with an average FWHM of  $\sim 4.36 \text{ \AA}$  (Seth et al. 2010). However, variations in the FWHM of  $\sim 10\%$  were found across the FOV. For this reason, the LSF was measured in each spaxel with the help of sky lines (as done, e.g., by Seth et al. 2010), in order to achieve more accurate kinematic measurements (see Section 4.2).

The data cube of NGC 205 used in this work was star subtracted by Nguyen et al. (2018) to minimize the impact of individual bright stars on the integrated kinematics. Their light was subtracted from the data cubes using PampelMuse (Kamann 2013), as explained in detail in Nguyen et al. (2018, 2019). Following the same procedure, we obtained a star-subtracted cube also for M 33.

While M 32 is located at a similar distance to NGC 205 and M 33, its very dense and bright NSC is crowded with individual stars as observed by NIFS. This made it impossible to use the same approach to subtract these individual stars.

#### 3.2. SINFONI Data

Observations of NGC 5102 and NGC 5206, performed with the Spectrograph for INtegral Field Observations in the Near

Infrared (SINFONI; Eisenhauer et al. 2003), were presented by Nguyen et al. (2018). We reanalyzed this data in a consistent way, and we added to the analysis new SINFONI observations for NGC 7793. SINFONI was mounted on the Unit Telescope (UT) 4 of the VLT and decommissioned in 2019. It offered AO-assisted observations (Bonnet et al. 2004), and the NGS mode was used for the corrections of our data cubes. SINFONI also has an FOV of  $3'' \times 3''$ , with a spaxel size of  $0''.05 \times 0''.1$ , covering a wavelength range from 1.1 to  $2.45 \mu\text{m}$ . Data reduction was performed using the ESO SINFONI pipeline, as explained in Neumayer et al. (2007) and Nguyen et al. (2018). The final cubes were obtained from a combination of several dithered exposures, after each one of them was corrected for the sky and telluric contaminations. Before being combined, SINFONI cubes were also corrected for additive residuals from the sky subtraction and velocity offsets between the individual data cubes, as explained in Nguyen et al. (2018).

The PSF was evaluated, with the same two-step procedure as for NIFS data (Section 3.1) but using two Gaussians for the fit, for NGC 5102 and NGC 5206 by Nguyen et al. (2018). F560W and F814W HST images were used, respectively, for the two galaxies. We derived the PSF for NGC 7793 following the same approach using an F153M-band HST image. PSF parameters are shown in Appendix D. SINFONI has a spectral resolution of  $R \sim 4000$ . Since its LSF does not fit a Gaussian function, its actual shape was measured by Nguyen et al. (2018) for NGC 5102 and NGC 5206, and in this work for NGC 7793. The same approach was used for the three galaxies, using OH sky lines, which can be approximated to delta functions. Therefore, the shape of these lines after reaching the detector is a good approximation of the LSF. In fact, the shape of one of these lines when observed with SINFONI appears to be more centrally peaked than a Gaussian and shows broader wings. In addition, since the SINFONI LSF varies across columns in the detector, this procedure was followed for each row in the sky frames. A median spectral resolution of  $6.32 \text{ \AA}$  was measured for NGC 7793.

#### 4. Methods for the Kinematic Analysis

We extract the nuclear stellar kinematics from NIFS and SINFONI data following a similar approach to Seth et al. (2008, 2010), Seth (2010), and Nguyen et al. (2018). They previously presented stellar-kinematic maps of the six published data cubes (see Section 3). For the sake of completeness and uniformity, we refitted the full sample using the setup described in this section. We used the range between  $2.285$  and  $2.390 \mu\text{m}$ , which includes the CO band-head absorption. This is the strongest absorption feature in galaxy spectra between 1 and  $3 \mu\text{m}$ . It is sharp and deep enough to be very sensitive to stellar kinematics. In this region of the spectrum, the effects of dust are minimized, and there is no emission from the sky (e.g., Silge & Gebhardt 2003).

##### 4.1. Voronoi Binning

We performed a Voronoi tessellation to spatially bin the reduced and combined NIFS and SINFONI cubes, making use of the VorBin Python package.<sup>10</sup> The Voronoi-binning method was described in Cappellari & Copin (2003) and consists of a two-dimensional adaptive spatial binning to a minimum signal-

to-noise ratio (S/N) around a target value. For NIFS data cubes, a variance cube was propagated through the data-reduction process. The S/N of each spaxel was calculated as the ratio between the mean measured flux ( $S$ ) and the square root of the mean variance spectrum ( $N$ ) in the selected wavelength range ( $2.285\text{--}2.390 \mu\text{m}$ ). For SINFONI data, with no available variance spectra, we used the mean measured flux ( $S$ ) and the standard deviation ( $N$ ) along the spectral direction, this time in the wavelength range between  $2.21\text{--}2.26 \mu\text{m}$ , with no significant absorption features. Prior to the Voronoi binning, we set a spaxel S/N threshold of 1 (in the wavelength range used for the analysis), so that all spectra with noise larger than the signal were not binned and discarded from the analysis.

We initially binned all galaxies to a target S/N of 25 in our wavelength range. Aiming at a compromise between a spatial resolution good enough to see structures and an acceptable quality of the spectra, we rebinned the nuclei with lower surface brightness (NGC 2403, NGC 2976, NGC 4244, and NGC 4449) to a target S/N of 15. We checked that decreasing the S/N did not have a negative impact on the spectral fitting and on the obtained kinematic parameters. Uncertainties (Section 4.4) were for  $S/N = 15$  similar or lower than for  $S/N = 25$ , in particular in the (central) region of the FOV where the Voronoi bins were smaller. Using this lower S/N allows us to recover rotation in some regions where it was blurred by larger bins. We still preferred to use  $S/N = 25$  for the rest of the galaxies, being more conservative when it comes to the goodness of the spectra especially in the outer regions, but reaching already a good compromise with spatial resolution. We show in Figure 2 three examples of Voronoi-binned spectra with different S/Ns.

##### 4.2. pPXF

We derived the kinematics of the 11 nuclei in our sample, using the Python implementation of the penalized pixel-fitting (pPXF) method<sup>11</sup> (Cappellari & Emsellem 2004; Cappellari 2017). This method selects and combines templates from a stellar library and convolves them with a line-of-sight velocity distribution (LOSVD) as a Gauss–Hermite series, to fit the observed spectra. We included in the fit the first four Gauss–Hermite moments and used an additive fourth-order polynomial. The “bias” pPXF parameter penalizes the higher moments of the LOSVD, when they are poorly constrained by the data. In that case, the LOSVD tends to a Gaussian, and the higher moments are biased toward zero. We used the default pPXF bias  $0.7\sqrt{500/N_{\text{goodpixels}}}$ , where  $N_{\text{goodpixels}} \lesssim 500$  is the number of spectral pixels left after masking the bad ones. This number, and then the bias-parameter value, slightly vary depending on the specific spectrum. The templates were convolved, to match the resolution of the observations, with the LSF measured for the specific Voronoi bin (see Section 3). This method provides us maps of mean velocity  $V$ , velocity dispersion  $\sigma$ , skewness  $h_3$ , and kurtosis  $h_4$ . We show in Figure 2 three different examples of pPXF fits. They include spectra from both instruments and with different S/Ns.

##### 4.3. Stellar Library

We initially fitted all galaxies with two different spectral libraries: the second data release (DR2) of the X-Shooter

<sup>10</sup> <https://pypi.org/project/vorbin/>

<sup>11</sup> <https://pypi.org/project/ppxf/>

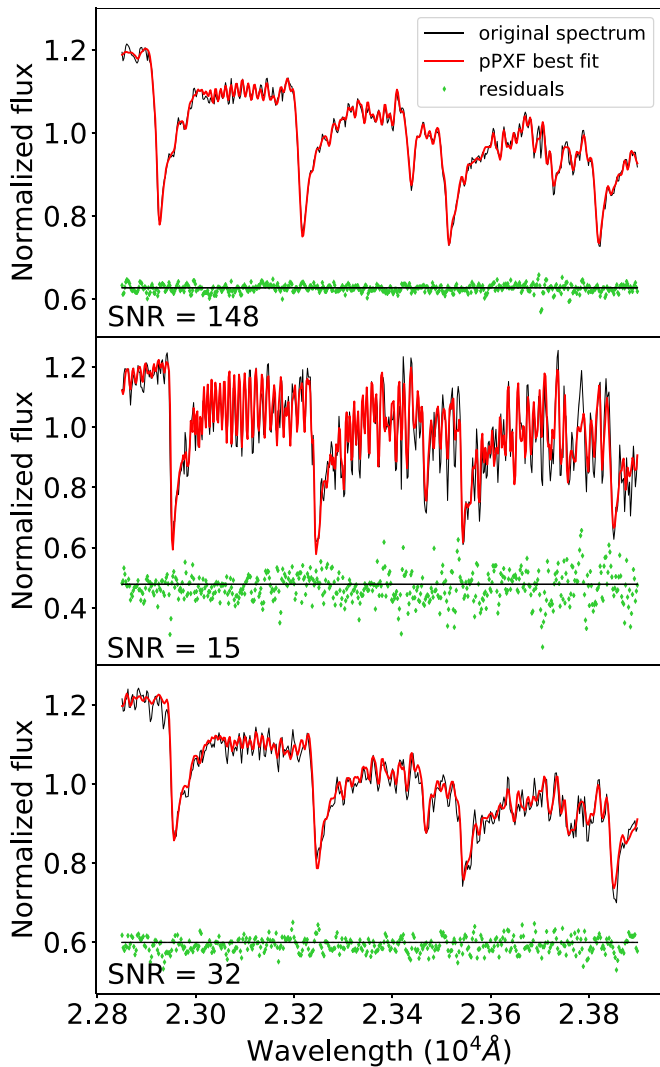


**Figure 2.** Examples of Voronoi-binned spectra and their pPXF best fits, for different cases. Top: M 32 NIFS spectrum with mean S/N of 148; middle: NGC 4449 NIFS spectrum, S/N  $\sim$ 15; bottom: NGC 7793 SINFONI spectrum, S/N  $\sim$ 32. Note that the lower values of  $\sigma$  in NGC 4449 (see Element 10 in the online figure set version of Figure 8) make a much larger number of absorption features visible in the middle spectrum than in the top and bottom ones. The observed spectrum is plotted in black, the best fit is plotted in red, and the residuals of the fit are plotted in green. The latter were calculated as the difference between the black and red spectra and arbitrarily shifted to fit in the plot.

Library (XSL; Gonneau et al. 2020) and the high-resolution spectra of cool stars from Wallace & Hinkle (1996; hereafter W&H). The XSL was designed to cover most of the Hertzsprung–Russell diagram and includes in total 813 spectra of 666 stars. It covers a large range of spectral types and chemical compositions. Repeated observations were performed for luminous cool stars that were expected to vary in time. The spectra cover three contiguous wavelength segments between  $\sim$ 300 nm and  $\sim$ 2.45  $\mu$ m, at a spectral resolution  $R \sim$  10,000. The W&H library, instead, provides eight suitable spectra of supergiant, giant, and main-sequence G- to M-type stars, of different luminosity classes, at  $R \sim$  45,000. This latter set of stars was used for the kinematic analysis by Seth (2010), Seth et al. (2010), and Nguyen et al. (2018).

The results obtained with the two spectral libraries were consistent between each other within the error estimates (Section 4.4). Therefore, the choice of the templates had to

be based on the balance between spectral resolution, much higher in W&H, and number of stars, much higher for the XSL. With slightly lower uncertainties in the results, we finally decided to adopt results from the XSL, based on the following considerations. According to Silge & Gebhardt (2003), the importance of using a library with a large number of stars resides in the available large variety of CO-band equivalent widths. Stars in the XSL were selected to map the widest possible ranges of stellar parameters such as effective temperature and surface gravity, closely related to the equivalent widths (Gonneau et al. 2020). Although W&H templates span a large range of equivalent widths in the CO bands (See Table 5 in Wallace & Hinkle 1996), the range covered by XSL is much more extended and better sampled.

All spectra in the DR2 of the XSL were corrected for instrument transmission, telluric absorption, and radial velocities and were provided in the rest frame (in air wavelengths; Gonneau et al. 2020). From the entire XSL, we picked only the spectra whose flux was corrected for slit losses (due to the narrow slit), since a non-corrected slope of the spectra might affect the full spectral fitting. We decided to include the repeated observations of variable stars, since they represent stars in different variability snapshots. We discarded the spectra with potential issues related to wavy continuum, artifacts or poor S/N in the K band, or superposition of other objects in the line of sight (LOS; as from Table B.1 in Gonneau et al. 2020). We finally gathered a set of 689 templates.

#### 4.4. Uncertainties from Monte Carlo Simulations

We estimated uncertainties for each of our kinematic parameters, by means of Monte Carlo (MC) simulations, as suggested by Cappellari & Emsellem (2004). We performed 1000 realizations for each one of the Voronoi bins. In each realization, we perturbed the observed spectra with wavelength-dependent random noise from a Gaussian distribution, since in real spectra, noise is not constant in the spectral direction. The standard deviation of the Gaussian was set from the variance spectra for NIFS observations, and from the residual spectrum (see Figure 2) for SINFONI data cubes (with no available variance spectra). We ran pPXF for each one of the 1000 perturbed spectra per Voronoi bin, now setting the bias parameter to 0.1. This allows for a more conservative estimate of errors as suggested by Cappellari & Emsellem (2004). Seth et al. (2014) and Nguyen et al. (2018) verified the robustness of errors obtained with this approach. Typical values of our uncertainties can be seen in all figures in Appendix A.

#### 4.5. Ordered Rotation vs. Random Motions

The ratio of ordered versus random motions ( $V/\sigma$ ) in galaxies reveals whether these systems are supported by pressure or by rotation and can provide insights about their formation and evolution. The anisotropy diagram, ( $V/\sigma$ ) as function of the observed ellipticity ( $\epsilon$ ), was first introduced by Illingworth (1977) and Binney (1978), to study whether there was a correlation between rotation and the apparent flattening of galaxies. The same diagram was later constructed for the 48 early-type galaxies in the Spectrographic Areal Unit for Research on Optical Nebulae (SAURON) sample (Cappellari et al. 2007). In addition, a new parameter  $\lambda_R$  was defined by Emsellem et al. (2007). It has a similar behavior to ( $V/\sigma$ ) but is

also sensitive to the spatial distribution of the velocity, and is a proxy of the projected specific angular momentum. Emsellem et al. (2007) introduced a new classification of early-type galaxies, into fast and slow rotators, based on  $\lambda_R$ . These same ( $V/\sigma$ ) and/or  $\lambda_R$  quantities were later measured for the larger samples of ATLAS<sup>3D</sup> (Emsellem et al. 2011), of Sydney-AAO (Australian-Astronomical-Observatory) Multi-object Integral-field Spectrograph (SAMI; van de Sande et al. 2017a) and Mapping Nearby Galaxies at Apache Point Observatory (APO) (MaNGA) galaxies (Graham et al. 2018; Greene et al. 2018). It was shown by the Calar Alto Legacy Integral Field Area Survey (CALIFA) collaboration how galaxies of different morphological types populate different regions of the ( $V/\sigma$ ) and  $\lambda_R$  versus  $\epsilon$  diagrams (Falc3n-Barroso et al. 2019). A review was given by Cappellari (2016).

These diagrams have been also used to provide an idea of whether NSCs are dominated by rotation or random motions (Lyubenova & Tsatsi 2019; Neumayer et al. 2020). In this work, we use them to investigate whether NSCs hosted by galaxies of different Hubble types lie in different regions of these diagrams in the same way as their host galaxies do. ( $V/\sigma$ ) gives a more intuitive way of quantifying the rotational support of a galaxy or an NSC, because it comes directly from the tensor virial equations (Binney 1978, 2005). However ( $V/\sigma$ ) gives relatively strong weights to the central part where the flux is usually at its peak. On the other hand  $\lambda_R$ , via its radial weighing (see Equation (2)), can distinguish central rotation from a more extended one, as well as being less dependent on inclination (Cappellari et al. 2007; Emsellem et al. 2007). For this reason we include both parameters in our analysis. We calculated ( $V/\sigma$ ),  $\lambda_R$ , and  $\epsilon$ , as luminosity-weighted averages over the area within the half-light ( $R_{e,\text{NSC}}$ ) elliptical isophote of the NSC, using the following definitions from Cappellari et al. (2007) and Emsellem et al. (2007):

$$\left(\frac{V}{\sigma}\right)_e = \sqrt{\frac{\sum_{i=1}^N F_i V_i^2}{\sum_{i=1}^N F_i \sigma_i^2}} \quad (1)$$

$$\lambda_{Re} = \frac{\sum_{i=1}^N F_i R_i |V_i|}{\sum_{i=1}^N F_i R_i \sqrt{V_i^2 + \sigma_i^2}} \quad (2)$$

$$\epsilon_e = 1 - \sqrt{\frac{\sum_{i=1}^N F_i y_i^2}{\sum_{i=1}^N F_i x_i^2}}. \quad (3)$$

We applied these equations on a spaxel-by-spaxel basis, on a total number of spaxels  $N$  within the  $R_{e,\text{NSC}}$  elliptical isophote.  $V_i$  and  $\sigma_i$  are, respectively, the velocity and the velocity dispersion of the  $i$ th spaxel (although calculated for the corresponding Voronoi bin; Section 4.2).  $F_i$  is the  $i$ th spaxel integrated flux in the original data cube.  $(x_i, y_i)$  are the coordinates of the spaxels, with the origin in the nuclear-kinematic center and rotated to be aligned, respectively, with the major and minor axis of the  $R_{e,\text{NSC}}$  elliptical isophote.  $R_i = \sqrt{x_i^2 + y_i^2}$  are the distances of spaxels from the center. We include in the calculation only spaxels within the  $R_{e,\text{NSC}}$  ellipse, i.e., the elliptical isophote with an area equal to the  $R_{e,\text{NSC}}$  circle ( $\pi R_{e,\text{NSC}}^2$ ). In general, the ( $V/\sigma$ ) and  $\lambda_R$  parameters are only rigorously meaningful for isolated systems and not subcomponents of galaxies. In the following, we will assume that NSCs are sufficiently dense, hence contrasted above the background and fully dominating the local gravitational potential and light, that they can be modeled as isolated

systems with good approximation (e.g., Hartmann et al. 2011). This will be further examined in Section 5.2.4.

We used the  $R_{e,\text{NSC}}$  in Table 1, except for NGC 5102. This nucleus was fitted by Nguyen et al. (2018) with two S3rsic components with effective radii of  $0''.1$  and  $2''.0$ . Our NGC 5102's kinematic maps do not cover the full region out to the integrated  $R_{e,\text{NSC}}$  of 1.6 arcsec. We chose instead an elliptical isophote of area equal to a circle of a radius of  $0''.6$  (Element 4 of the online figure set for Figure 8). We aimed at finding a compromise between a significant coverage of the FOV and not too large  $V$  and  $\sigma$  uncertainties. The selected radius allows us to include Voronoi bins with uncertainties lower than  $17 \text{ km s}^{-1}$  and  $20 \text{ km s}^{-1}$ , respectively, for  $V$  and  $\sigma$ , in 90% of the included spaxel. For NGC 4244, we gave in Table 1 the  $R_{e,\text{NSC}}$  of the two S3rsic components used to fit the NSC. For the calculations, we used the arithmetic mean of the two values ( $R_{e,\text{NSC}} = 5.43 \text{ pc}$ ).

Uncertainties for ( $V/\sigma$ )<sub>e</sub>,  $\lambda_{Re}$ , and  $\epsilon_e$  were calculated via MC simulations. We performed here 500 realizations adding random Gaussian noise to the parameters in Equations (1), (2), and (3). Each  $V_i$  and  $\sigma_i$  was perturbed with a noise of the level of their corresponding uncertainties (see Section 4.4 and the online figure set for Figure 8). For  $F_i$ , we took the mean standard deviation of each spectrum (as used in Section 4.4). For  $x_i$ ,  $y_i$ , and  $R_i$ , we introduced some noise in the parameters used for their rotation and centering. For the position angle of the  $R_{e,\text{NSC}}$  ellipse, we took the uncertainties from the isophote fitting, while for the position of the kinematic center, we estimated an error of 1 spaxel.

## 5. Results

### 5.1. Kinematic Maps

For each nucleus in our sample, individual maps of the first four moments of the LOSVD and their uncertainties are shown and discussed in Appendix A. Our kinematic results are in excellent agreement with the previously published maps obtained with the same data sets of M 32 (Seth 2010), NGC 404 (Seth et al. 2010), NGC 4244 (Seth et al. 2008), NGC 205, NGC 5102, and NGC 5206 (Nguyen et al. 2018). Rotation is observed in all nuclei in our sample, independently of whether the host galaxy is an early or a late type. Sometimes this rotation is strong as in M 32, NGC 4244, and NGC 5102, with a maximum velocity between 30 and  $60 \text{ km s}^{-1}$ , while in others it is not as significant (e.g., NGC 205 and NGC 4449 do not reach  $10 \text{ km s}^{-1}$ ). Some early-type galaxies display complex kinematic structures in their nuclear regions. This is the case of NGC 404, whose NSC is made up of two components: the most extended shows clear rotation, while the inner component counter-rotates (see Appendix A for more details). In NGC 205, we observe an offset between the rotation axis and the minor axis of the nucleus, perhaps suggesting the presence of a merger component.

Regarding the velocity dispersion in the very central region, we observe different behaviors that are clearly related to the mass of the central black hole (BH). M 32 and NGC 5102, with supermassive black holes (SMBHs) of about  $10^6 M_\odot$  (e.g., Seth 2010; Nguyen et al. 2018), show a strong  $\sigma$  peak in their centers. In most of our nuclei, with a BH mass of about  $10^5 M_\odot$  (see Appendix A), we observe higher  $\sigma$  values in the central region but without a defined peak. Finally, we have a central drop for low BH masses ( $<10^4 M_\odot$ ) or no BH detections (in

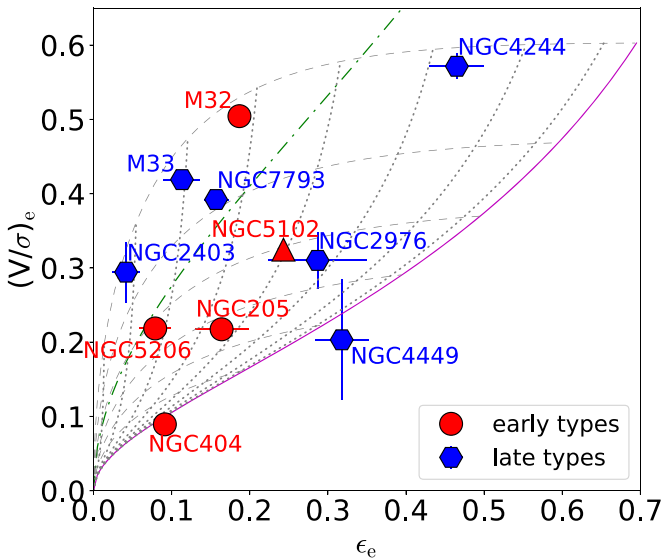


**Figure 3.**  $(V/\sigma)_e - \epsilon_e$  diagram for the sample of 11 nuclei studied in this work. Both  $(V/\sigma)_e$  and  $\epsilon_e$  were integrated within the  $R_{e,\text{NSC}}$  ellipse. Nuclei hosted by early-type galaxies are indicated with red circles while the ones hosted by late-type galaxies are shown by blue hexagons. The names of the host galaxies are indicated closely to the individual points. The upward triangle indicates a lower limit for NGC 5102, where the  $R_{e,\text{NSC}}$  ellipse was not fully covered. The green dashed-dotted and magenta solid lines are indicated as a reference, and they refer to edge-on galaxies. They correspond, respectively, to isotropic oblate rotators from Binney (2005) and to galaxies with  $\delta = 0.7\epsilon_{\text{intr}}$  as from Cappellari et al. (2007). The dotted gray lines show how galaxies with  $\delta = 0.7\epsilon_{\text{intr}}$  move from the magenta line when inclination is decreased. Different lines are separated by steps of  $10^\circ$  in inclination, from edge-on (on the magenta line) to face-on. Different dashed gray lines correspond to galaxies with different intrinsic ellipticities, from 0.195 (bottom) to 0.695 (top), and with  $\delta = 0.7\epsilon_{\text{intr}}$ .

M 33, NGC 205, and NGC 2976). A similar correlation of the central velocity dispersion with the BH mass was suggested, e.g., by dynamical modeling of GCs and ultra-compact dwarf galaxies (UCDs; Voggel et al. 2018; Aros et al. 2020). On the other hand, galaxies with an SMBH do not show necessarily a central peak of velocity dispersion. The observed LOS  $\sigma$  depends as well on BH-unrelated factors, such as the galaxy mass and light distributions, the spatial resolution, and the radial anisotropy (see also, e.g., McConnell et al. 2012).

Due to the penalization against poorly constrained nonzero values of  $h_3$  and  $h_4$ , introduced by pPXF (Section 4.2), a good determination of these higher moments requires a higher S/N than for  $V$  and  $\sigma$ . We obtain good  $h_3$  and  $h_4$  maps only for some nuclei in our sample. Interestingly, we see an  $h_3 - V$  anticorrelation in some of the galaxies (M 32, M 33, NGC 404, NGC 4244, and NGC 5102). This anticorrelation is usually observed in disklike rotating structures, when superimposed in the LOS on slower or nonrotating components (van der Marel & Franx 1993; Bender et al. 1994; Krajnović et al. 2008; Guérou et al. 2016; Pinna et al. 2019). For the rest of this discussion, we focus on the more robust  $V$  and  $\sigma$  measurements.

### 5.2. $(V/\sigma)_e$ and $\lambda_{\text{Re}}$ Diagrams and Their Interpretation

The radial distribution of  $|V|/\sigma$  is shown in Appendix B for each one of the 11 nuclei in our sample. Measurements of  $\epsilon_e$ ,  $(V/\sigma)_e$ , and  $\lambda_{\text{Re}}$  for our full sample are gathered in Table 2 (Appendix C).  $(V/\sigma)_e$  and  $\lambda_{\text{Re}}$  are plotted as functions of  $\epsilon_e$ , respectively, in Figures 3 and 4. Nuclei of early-type hosts are indicated in red, and the late-type ones in blue. We show in

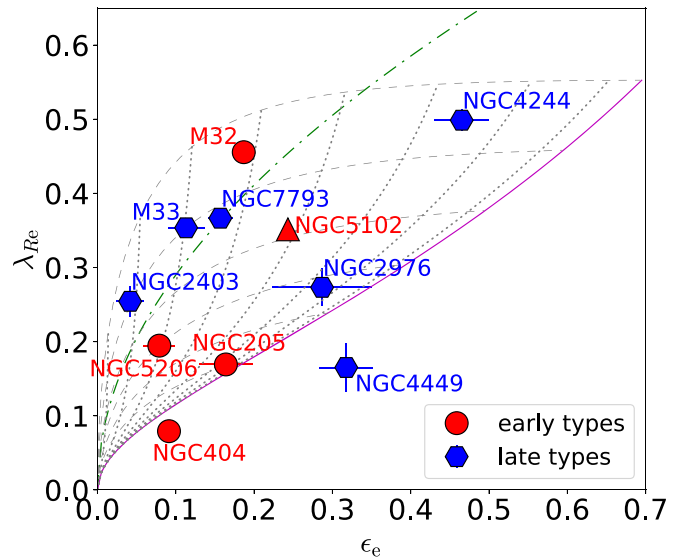


**Figure 4.**  $\lambda_{\text{Re}} - \epsilon_e$  diagram for the sample of 11 nuclei studied in this work. Both  $\lambda_{\text{Re}}$  and  $\epsilon_e$  were integrated within the  $R_{e,\text{NSC}}$  ellipse. Symbols, lines, and colors are the same as in Figure 3.

Figures 3 and 4 different lines, which were introduced for galaxies, as a reference to guide the reader’s eye. The magenta solid line is an approximation for edge-on galaxies with  $\delta = 0.7\epsilon_{\text{intr}}$ , where  $\delta$  is the velocity anisotropy parameter (Binney & Tremaine 1987, Section 4.3) and  $\epsilon_{\text{intr}}$  is the intrinsic ellipticity. This line is in general the lower envelope of observed rapidly rotating galaxies and was introduced by Cappellari et al. (2007). Lower inclinations move the magenta solid line toward the left side, as indicated by the gray dotted lines. Each gray dashed line corresponds to a value of  $\epsilon_{\text{intr}}$  and goes, decreasing inclination, from the magenta solid line toward the origin. The green dashed-dotted line corresponds to “edge-on isotropic oblate rotators” ( $\delta = 0$ ). It was introduced by Binney (1978) and updated for integral-field data in Binney (2005). Other roughly parallel lines toward higher  $\epsilon_e$  would correspond to edge-on oblate galaxies with increasing velocity anisotropy  $\delta$ .

As expected from the tight relation between  $(V/\sigma)_e$  and  $\lambda_{\text{Re}}$  (Emsellem et al. 2007, 2011), the sample is distributed in a very similar way in Figures 3 and 4. Five of the six nuclei hosted by late-type galaxies are distributed in the upper regions of the diagrams (above 0.25). Our five nuclei of early types are distributed all over the ranges of  $(V/\sigma)_e$  and  $\lambda_{\text{Re}}$ , with three out of five points below 0.25. Therefore, on average, early-type galaxies in our sample show lower nuclear  $(V/\sigma)_e$  and  $\lambda_{\text{Re}}$  than late types. Nuclei in early-type galaxies also display a lower average  $\epsilon_e$  than late types, with values below 0.3 for the full subsample while the highest nuclear ellipticities correspond to late types.

However, these average trends have to be considered with caution. First, the contrast of nuclei with respect to the underlying light components may be lower in early-type galaxies than in late types, having a larger bias on  $(V/\sigma)_e$  and  $\lambda_{\text{Re}}$  values (see Section 5.2.4). This is the case for NGC 404, the lowest point in the diagrams and the one with the largest contamination from the host galaxy. This nucleus is moreover characterized by other peculiarities. The low  $(V/\sigma)_e$  and  $\lambda_{\text{Re}}$  (measured within  $R_{e,\text{NSC}}$ ) result from the LOS integration of two counter-rotating structures (see Section 5.1 and Appendix A). This nucleus (and the host) has also a low



inclination, with a potential impact on the measured  $\epsilon_e$ ,  $(V/\sigma)_e$ , and  $\lambda_{R_e}$  (Section 5.2.1). If we considered this point as an outlier, early- and late-type galaxies would have a similar  $(V/\sigma)_e$  and  $\lambda_{R_e}$  distribution.

The three early-type nuclei in the bottom-left corner of the diagrams are characterized by slow observed rotation. Not only NGC 404 but also NGC 205 display complex kinematic structures. The nuclei of NGC 205 and NGC 5206, with similar  $(V/\sigma)_e$  and  $\lambda_{R_e}$ , show both slow rotation and low ellipticity. While also in the nucleus of NGC 205, we show evidence of different kinematic components; this is not found in NGC 5206 (Appendix A). Finally, there is one last point in the lower regions of Figures 3 and 4. NGC 4449, a late-type galaxy with low S/N in our nuclear observations and large error bars in the measured kinematic parameters, displays  $(V/\sigma)_e$  and  $\lambda_{R_e}$  values similar to NGC 205 and NGC 5206. However, if we considered this point as an outlier, the trend with late-type galaxies covering the upper region of the diagrams, and early types being located all over the plane, would be much more clear.

Finally, two of the early-type nuclei lie in the region dominated by late types. They are hosted by M 32 and NGC 5102 and both show a strong disklike rotation (and a  $\sigma$  peak in the center). Moreover, NGC 5102's plotted values of  $(V/\sigma)_e$  and  $\lambda_{R_e}$  should be considered lower limits, as discussed later in Section 5.2.2. We consider M 32 and NGC 5102 two peculiar cases, as it is known from previous studies that they were spirals in the past (see Appendix A). Their NSCs probably bring the kinematic footprint of their former late-type host and therefore show similar properties to nuclei of late-type galaxies. This will be discussed in greater detail in Section 6.1.

We now discuss some of the impacts that complicate the interpretation of our  $(V/\sigma)_e$  and  $\lambda_{R_e}$  diagrams.

### 5.2.1. Inclination

The impact of inclination on the measured values of  $V$  (therefore on  $(V/\sigma)_e$  and  $\lambda_{R_e}$ ) and  $\epsilon_e$ , already tested by Emsellem et al. (2007) and Emsellem et al. (2011), is illustrated, respectively, by the gray dotted and dashed lines in Figure 3 and 4, referring to galaxies with  $\delta = 0.7\epsilon_{\text{intr}}$ . They show that  $\epsilon_e$  is more affected by inclination in the upper half of the diagrams, while  $(V/\sigma)_e$  and  $\lambda_{R_e}$  are more affected in the leftmost region. However, each gray dotted line spans a large range of  $(V/\sigma)_e$  and  $\lambda_{R_e}$  (and  $\epsilon_e$ ), indicating that inclination alone cannot explain the distribution of the global sample in the upper and lower regions of the diagrams.

Assuming that both NGC 4244 and its nucleus are seen edge-on (Hartmann et al. 2011), inclination might be the main driver for the fact that this nucleus is located in the top-right regions of Figures 3 and 4. NGC 404, the least-inclined galaxy in our sample ( $\sim 11^\circ$ ; del R o et al. 2004), hosts a nucleus that is located in the bottom-left corner. Apart from the two extreme cases, the rest of the hosts have intermediate-to-high inclinations with no clear correlation with the values of  $(V/\sigma)_e$  and  $\lambda_{R_e}$ . Nuclei in the bottom region (e.g., the one in NGC 205, with inclination  $\sim 59^\circ$ ; Nguyen et al. 2018) are not necessarily the ones with the lowest inclinations. The fact that the nucleus hosted by NGC 5206 ( $\sim 44^\circ$  inclined; Nguyen et al. 2018) is located in Figure 3 close to the same dashed line as the one in NGC 5102 ( $\sim 72^\circ$  inclined; Nguyen et al. 2018) may suggest that the two galaxies have similar intrinsic levels of rotations but are observed at different inclinations. However, this does

not happen in Figure 4, where these two galaxies lie close to (dashed) lines with different intrinsic ellipticities.

Some blue hexagons, mostly in the upper half of the diagrams, correspond to relatively low host inclinations. An example is M 33's nucleus, whose trajectory in the  $(V/\sigma)_e - \epsilon_e$  diagram if projected from its inclination ( $\sim 49^\circ$ ; assumed to be the same as the host galaxy) to the edge-on view was shown by Hartmann et al. (2011) in their Figure 5. The nuclei of M 33 and NGC 2403, which are very similar galaxies (see Appendix A), lie relatively close to each other in the diagrams, and their offset might be explained at least partially by their different inclinations (independently of NGC 2403's inclination, its nucleus shows almost round isophotes in Element 7 in Figure 8).

### 5.2.2. Integration Aperture

The integration aperture also has an impact on measured values of  $\epsilon$ ,  $(V/\sigma)$ , and  $\lambda_R$  (e.g., Emsellem et al. 2007, 2011). In galaxies, a larger integration radius corresponds in general to a larger  $\lambda_R$ . However, this depends on the specific structure of galaxies, and later-type galaxies with an underestimated  $R_e$  may lie in the same region of the  $\lambda_{R_e}$  diagram as galaxies with a larger bulge but with an overestimated  $R_e$  (Harborne et al. 2019). Similarly, more disklike NSCs with an underestimated  $R_{e,\text{NSC}}$  might lie in the same region as more spherical or more slowly rotating NSCs with an overestimated  $R_{e,\text{NSC}}$ . At the same time, an overestimate of  $R_{e,\text{NSC}}$  would lower the contrast of the NSC with respect to the underlying galaxy, affecting the self-consistency of the measurements (Section 5.2.4).

For NGC 5102, we used an aperture smaller than the  $R_{e,\text{NSC}}$  ellipse, because the latter was not entirely covered by our data. We also choose an ellipse that did not take into account the very outer Voronoi bins with large errors (Section 4.5). Therefore, we expect a bias toward lower values in our measurements of  $(V/\sigma)_e$  and  $\lambda_{R_e}$ . Aperture corrections were proposed by van de Sande et al. (2017b) to quantify this kind of bias for the SAMI and ATLAS<sup>3D</sup> galaxy surveys. However, as these corrections are PSF dependent and have only been applied to galaxies, they are likely inappropriate for NSCs. Thus we chose to conservatively treat the non-aperture corrected values of NGC 5102 as lower limits and to indicate them with upward triangles in Figures 3, 4, 6, and 7.

### 5.2.3. PSF Effects

Kinematic measurements are known to be affected by the PSF when this is of the order of the characteristic size of the galaxy (van de Sande et al. 2017a; Graham et al. 2018; Greene et al. 2018; Harborne et al. 2019, 2020). Beam smearing and atmospheric seeing result in observed lower rotation velocity and higher velocity dispersions in the central region of the FOV. Therefore, measurements of  $(V/\sigma)_e$  and  $\lambda_{R_e}$  are in general biased toward lower values. The impact of seeing is larger at scales comparable to the PSF and for galaxies with a higher amount of rotation (van de Sande et al. 2017a; Graham et al. 2018; Harborne et al. 2019).

Harborne et al. (2020) proposed analytic corrections to estimate the impact of the PSF in observational measurements of  $(V/\sigma)_e$  and  $\lambda_{R_e}$  in galaxies (Appendix D). While detailed modeling should be done in order to assess whether these corrections apply to the specific regime of galactic nuclei, and they might not be fully appropriate for a quantitative analysis, they provide a qualitative idea of the PSF effect. We have used

them to estimate how important this impact is in our measurements. We include the details of the calculations and the results in Appendix D. The PSF corrections shift all nuclei upward in the  $(V/\sigma)_e$  and  $\lambda_{R_e}$  plots (Figures 10 and 11 in Appendix D). This effect is stronger for nuclei hosted by late-type galaxies (an increase of  $\sim 60\%$ ) than for those in early types ( $\sim 40\%$ ; see also Table 2 in Appendix C). NGC 205 is an exception, with the largest PSF impact among early-type galaxies, mainly due to the small size of its NSC relatively to the PSF size. Nevertheless, the points remain similar in relative position to each other, and thus this correction does not significantly affect our conclusions.

#### 5.2.4. The Impact of the Underlying Galaxy

Our method is based on an LOS-integrated analysis of kinematics. Since NSCs are embedded in their host galaxy, kinematic measurements in the nuclear region are affected by all other components in the LOS. In this paper, we assume that the light from the NSC fully dominates the region within its  $R_{e,NSC}$ , and therefore the bias of our measurements due to the underlying galaxy is not significant.

We first tested this by deriving both the local (surface-brightness) and integrated (within an aperture) radial flux profiles of the NSCs relative to the background galaxy. For such an experiment, we used the surface-brightness decomposition as available via Seth et al. (2010), Carson et al. (2015), and Nguyen et al. (2018; as from the rightmost column in Table 1). In Figure 5, we show the ratio of the local and integrated fluxes between the NSC and the background, for all galaxies in our sample except NGC 4449, with no surface-brightness profiles available in the literature. Within  $1 R_{e,NSC}$ , those ratios are almost all above a value of 10, while only NGC 404 shows a ratio around 3 at that radius. This confirms that the NSCs fully dominate both the local and integrated flux budget within the  $1 R_{e,NSC}$  apertures.

The level of contamination on the measured values of  $\lambda_{R_e}$  and  $(V/\sigma)_e$  depends on many parameters, including the gradient of the potential assumed for the background, the mass ratio between the two components, the compactness of the NSC, the mass-to-light ratio (as both the potential and the luminosity weighing play a role), and obviously the dynamical status of each component (their relative  $V$  and  $\sigma$  values, which spatially vary). We performed a simplified calculation taking into account the weighing of each component in the derivation of  $\lambda_{R_e}$  (or  $(V/\sigma)_e$ ) but assuming a rather constant luminosity for the background. This shows that when these ratios stay above a value of 10, the contamination from the host potential and light is relatively little, at the level of 10% to 15% (assuming mass follows light within  $R_{e,NSC}$ ). For NGC 404, the contamination may be higher, and we estimate, again using the same simple assumptions, that it amounts to a maximum of 40%.

To check such a naive calculation, we further produced mock kinematic models of the central region of three targets in our sample, namely NGC 404, M 32, and NGC 7793, representing the two worst as well as one of the best cases, respectively, in terms of the NSC contrast. We thus directly examined the impact of embedding the NSC into the potential well of a host galaxy, by comparing the resulting measures of  $(V/\sigma)_e$  and  $\lambda_{R_e}$  in the ideal case of an “isolated” self-gravitating NSC, and of the same NSC within its late-type host.

We first modeled the mass distribution of the three galaxies via multi-Gaussian expansions (MGEs; Emsellem et al. 1994;

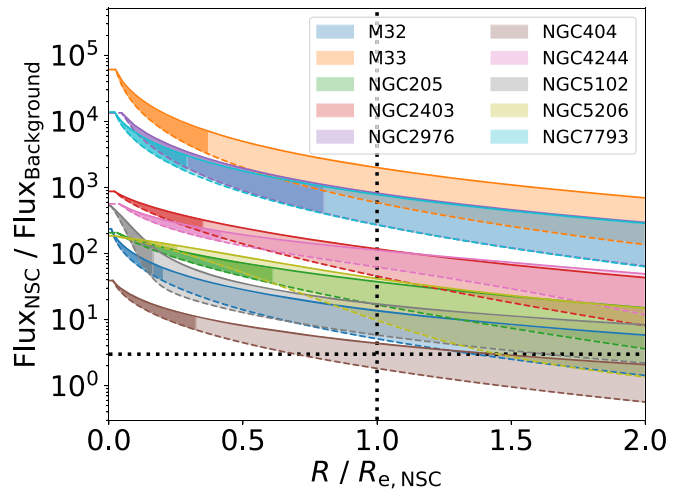


**Figure 5.** Contrast between the NSCs and the background flux for each galaxy in our sample (except NGC 4449), illustrated by the radial profiles of the ratio between the surface brightness of the two components. Each galaxy is represented by an individual color. The shaded areas are limited by an upper (lower) curve corresponding to the ratio of the integrated (local) flux. The darker shaded areas are added to represent the radius of the half-width at half-maximum, of the PSF for each galaxy observation. The vertical dotted line shows the  $1 R_{e,NSC}$  radius, while the horizontal dotted line is just indicative of a factor of three ratio.

Cappellari 2002). For NGC 404, we made use of the model published by Nguyen et al. (2017). For M 32, we used the MGE model by Verolme et al. (2002), and for NGC 7793, we built a model based on an image from the Two Micron All Sky Survey (2MASS) Large Galaxy Atlas (Jarrett et al. 2003). We then predicted the projected nuclear kinematics ( $V$ ,  $\sigma$ ) assuming axisymmetry and a fixed inclination and computed the respective integrated  $\lambda_R$  (and  $(V/\sigma)$ ) radial profiles. As expected, when adding the underlying galaxy background potential (and light) to the NSC, measurements tend to higher or lower values depending on the dynamical state of these background stars. Again, the impact naturally depends on both the local fraction of light corresponding to the NSC and on its integrated weight within the selected aperture.

As expected, the effect is negligible for  $\lambda_R$  and  $(V/\sigma)$  values within radii where the NSC fully dominates with contrast ratios above 10, while it becomes significant for ratios below 5. For both NGC 7793 and M 32, the contamination ( $\Delta\lambda_R$ ) is less than 10%, while for NGC 404, it is just below 20%. An interesting twist pertaining to the case of NGC 404 is that the nuclear region includes clear stellar counter-rotation, which, together with its low inclination, tend to make its observed  $\lambda_R$  value quite low. The photometric decomposition used in the above-mentioned modeling assumes that the NSC is a mixture of co- and counter-rotating stars, and has a very strong azimuthal anisotropy (lowering its mean stellar velocity). If we were to assume that the NSC comprises only the most central counter-rotating stars, it would maximize its mean velocity while increasing then the relative anisotropy difference between the NSC and the host, and would in turn very significantly emphasize the contamination.

Overall, we therefore conclude that our  $\lambda_{R_e}$  and  $(V/\sigma)_e$  are not significantly affected by such a contamination effect, except possibly for NGC 404, which has a complex kinematic structure (del Río et al. 2004; Bouchard et al. 2010), and quite a low inclination.

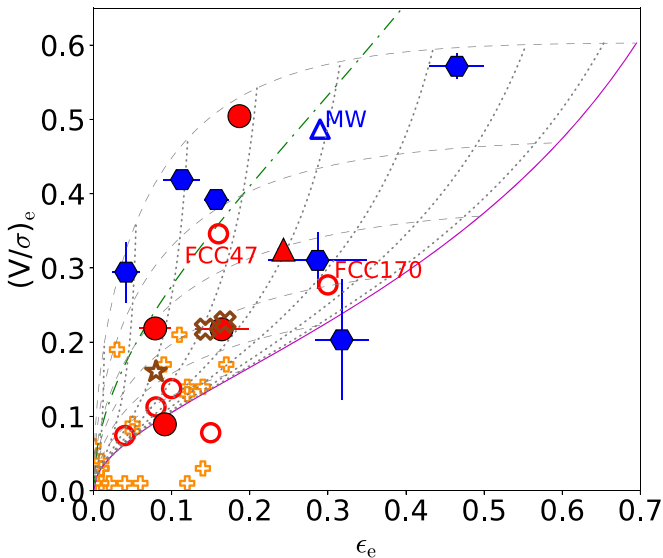


**Figure 6.** Comparison of our sample of 11 nuclei (filled points, as from Figure 3) with points from previous works (open points), in the  $(V/\sigma)_e - \epsilon_e$  diagram. Red open circles correspond to nuclei hosted by early-type galaxies analyzed by Lyubenova & Tsatsi (2019). The open blue upward triangle corresponds to a lower limit for the Milky Way (MW; Feldmeier et al. 2014). Orange open plus symbols correspond to GCs from Kamann et al. (2018). M 54 (Alfaro-Cuello et al. 2020) is indicated with a brown star, and the two UCDs M 59-UCD 3 (Ahn et al. 2018) and M 60-UCD 1 (Seth et al. 2014) are indicated with brown open “X” symbols. The green dashed-dotted and the magenta solid lines are the same as in Figure 3.

### 5.3. Previous Samples in the Literature

We added previously observed NSCs, GCs, and UCDs, with available kinematics in the literature, to the  $(V/\sigma)_e - \epsilon_e$  and  $\lambda_{Re} - \epsilon_e$  diagrams. In Figures 6 and 7, we compare our results with a sample of six nuclei from Lyubenova & Tsatsi (2019), indicated with red open circles, and with measurements from Feldmeier et al. (2014) for the NSC in our Galaxy, indicated as a blue open upward triangle. We also included in the diagrams a sample of GCs in the Milky Way (MW) from Kamann et al. (2018; indicated as orange open plus symbols), the nucleus of the Sagittarius dwarf galaxy, M 54, from Alfaro-Cuello et al. (2020; brown open star), and two UCDs, M 59-UCD 3 from Ahn et al. (2018) and M 60-UCD 1 from Seth et al. (2014; brown open “X” symbols).

#### 5.3.1. Other Galactic Nuclei

We compare here our sample with the six nuclei whose kinematics was studied by Lyubenova & Tsatsi (2019). They are hosted by early-type galaxies in the Fornax cluster, and thus they live in a higher-density environment. They are more than five times more distant than our sample (about  $\sim 20$  Mpc from us). While this leads to a more limited physical resolution than in our sample, we have a similar number of Voronoi bins, within the  $R_{e,\text{NSC}}$ , to some of our galaxies. The galaxies in this sample have also, on average, larger masses than ours. Lyubenova & Tsatsi (2019) extracted the nuclear kinematics, from AO-assisted SINFONI data, using a very similar approach to ours. On the other hand, they estimated  $\epsilon_e$  from isophotal fitting within  $R_{e,\text{NSC}}$ .

Similar to the early-type galaxies in our sample, most of the nuclei in their sample are round and do not rotate strongly, as shown in Figures 6 and 7. Four out of six have  $(V/\sigma)_e < 0.25$ ,  $\lambda_{Re} < 0.2$ , and  $\epsilon_e < 0.2$  and are actually located in the diagrams

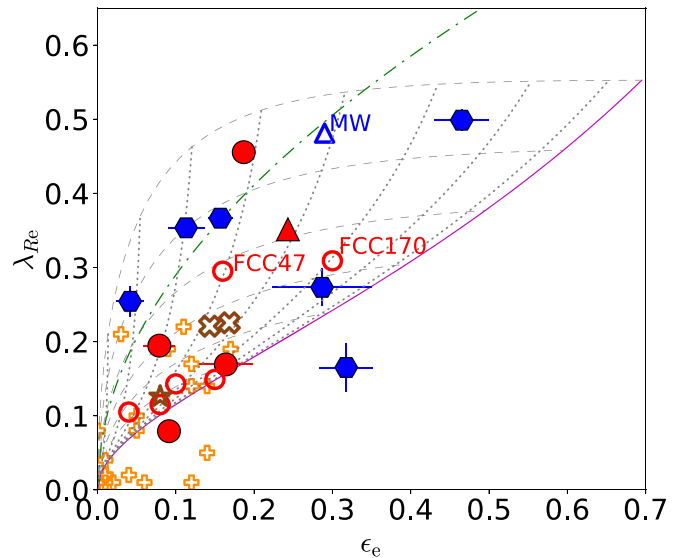


**Figure 7.** Comparison of our sample of 11 nuclei with points from previous works, in the  $\lambda_{Re} - \epsilon_e$  diagram. Symbols, lines, and colors are the same as in Figure 6.

close to the lowest points in our sample (especially to NGC 404). These points strengthen the trend, with nuclei in early-type galaxies being located in a lower region of the diagrams with respect to the ones hosted by late types. However, caution is needed regarding this trend since early-type galaxies from Lyubenova & Tsatsi (2019) are different objects from galaxies in our sample. As mentioned, they are more massive and live in a much denser environment, which implies accelerated mass assembly and early quenching (e.g., Fujita & Nagashima 1999). On the other hand, just as with our sample, there are two exceptions of strongly rotating nuclei hosted by early-type galaxies: FCC 47 and FCC 170. These nuclei have peculiar properties that might be the cause for their location in the diagrams. Their origin is discussed in Section 6.

We calculated  $(V/\sigma)_e$  and  $\lambda_{Re}$  for the NSC in the MW, using values of  $V$  and  $\sigma$  from Feldmeier et al. (2014). Their radial coverage was slightly smaller than  $R_{e,\text{NSC}}$ ; therefore, this point should be considered as a lower limit and is indicated as an upward triangle in Figures 6 and 7. The ellipticity (0.29) was taken from Schödel et al. (2014). The NSC in the MW lies in the upper region of the diagrams, providing additional evidence that late-type nuclei are, on average, more rotation dominated than early-type nuclei. While the MW is more massive than galaxies in our sample, with a stellar mass of  $\sim 6 \times 10^{10} M_\odot$  (Licquia & Newman 2015), and hosts an SMBH of  $\sim 4 \times 10^6 M_\odot$  (Gillessen et al. 2017), the mass of its NSC is similar to the most massive NSCs in our sample (hosted by M 32 and NGC 5102; see Appendix A). With a quite typical  $R_{e,\text{NSC}} \sim 4.2$  pc, the MW NSC has a relatively high mass of  $1.4\text{--}2.5 \times 10^7 M_\odot$  (Feldmeier et al. 2014; Schödel et al. 2014; Feldmeier-Krause et al. 2017b). In Figures 6 and 7, it is located relatively close to massive nuclei in our sample. We discuss in Section 6 the potential formation scenario of the NSC in our Galaxy.

#### 5.3.2. Globular Clusters and Ultra-compact Dwarfs

GCs are connected to NSCs in different ways, although they are systems with different intrinsic properties, and they reside in different regions of the potential well of galaxies. The

relationship between NSCs and GCs is rather complex: they could form in a similar way, NSCs could form from GC accretion, and/or GCs could be stripped galaxy nuclei. To facilitate a comparison, we included in our discussion a sample of 21 MW GCs with published  $(V/\sigma)_e$  and  $\lambda_{R_e}$  (Kamann et al. 2018; ellipticities from Harris 1996). The full GC sample in Figures 6 and 7 lies in the region where most nuclei hosted by early-type galaxies are concentrated, perhaps suggesting a potential evolutionary connection with these NSCs (see Section 6).

We have added to our diagrams M 54, an object straddled between NSCs and GCs and with available kinematics. It is the second most massive GC of the MW, and the stripped nucleus of the disrupted Sagittarius dwarf spheroidal galaxy (Bellazzini et al. 2008; Mucciarelli et al. 2017; Alfaro-Cuello et al. 2019; see discussion in Section 6.5). We calculated  $(V/\sigma)_e$  and  $\lambda_{R_e}$  for M 54 from the kinematics published by Alfaro-Cuello et al. (2020), approximating a constant flux per spatial bin within the effective radius. This point is located, in Figures 6 and 7, in the region dominated by NSCs in early-type galaxies and by the more rapidly rotating GCs.

Finally, we included in our analysis the two UCDs M 59-UCD 3 and M 60-UCD 1, for which the kinematics is available, respectively, from Ahn et al. (2018) and Seth et al. (2014). We added these two points to Figures 6 and 7, integrating within the effective radius of the inner morphological components of these UCDs, which are thought to be the NSCs of the progenitor galaxies. These points are actually located, in our diagrams, on the top of the early-type dominated region, where the fastest rotating GCs are found.

## 6. Discussion

While some amount of rotation was observed in all nuclei in our sample, they are distributed in different regions of the  $(V/\sigma)_e$  and  $\lambda_{R_e}$  diagrams. Overall, our results suggest that most NSCs in late-type galaxies are rapidly rotating, while those in early-type galaxies have on average less rotation. In this section we discuss how these observations translate to constraints on NSC formation. We first consider the interpretation of galaxy kinematics in the context of their formation to see if analogous formation mechanisms may be at work in NSCs. Emsellem et al. (2007) suggested that gas and mergers play a key role in the formation and evolution of, respectively, rapidly and slowly rotating early-type galaxies. Greene et al. (2018) found that an important fraction of high-mass early-type galaxies has high angular momentum, and they differ from slow rotators in their (larger) amount of ionized gas. The importance of gas, either provided via simple accretion or wet mergers, to keep and/or increase the angular momentum of a galaxy, was also shown in simulations (e.g., Lagos et al. 2018; Walo-Martín et al. 2020).

If we qualitatively extrapolate this interpretation to galactic nuclei, their location in the  $(V/\sigma)_e$  and  $\lambda_{R_e}$  diagrams might be determined by the balance between the two most invoked NSC formation mechanisms: in situ formation from gas inflow and inspiralling of star clusters. While they might have both played a role in the formation of the same NSC, we use our sample to test a scenario where a more dominant contribution of in situ star formation, with respect to star-cluster infall, would correspond to larger values of  $(V/\sigma)_e$  and  $\lambda_{R_e}$ . However, we have to be cautious to avoid too simplistic interpretations. The full picture needs to include other possibilities such as the accretion of gas-rich clusters (Guillard et al. 2016) or the

accretion of clusters with high angular momentum, such as the ones in Lahén et al. (2020).

Appendix A contains, for each individual nucleus in our sample, a detailed description of the kinematics from our results, as well as a review of previous studies regarding both NSCs and host galaxies. In this broader context, a short discussion on the potential formation scenario for each NSC is also provided. We therefore summarize and further discuss here the information contained in Appendix A.

### 6.1. The Formation of Higher-angular-momentum NSCs

In our sample, galactic nuclei in late-type galaxies show on average higher values of  $(V/\sigma)_e$ ,  $\lambda_{R_e}$ , and  $\epsilon_e$ . This is in agreement with in situ formation playing a leading role in the formation of these NSCs, hosted by a type of galaxy that is in general characterized by ongoing star formation.

As recently suggested for early-type galaxies by Fahrion et al. (2021), gas accretion and subsequent in situ formation might be needed for the growth of massive NSCs ( $\gtrsim 10^7 M_\odot$ ). However, this may happen in all types of galaxies (see also Neumayer et al. 2020). The four most massive NSCs in our sample, with masses larger than  $10^7 M_\odot$  (see Appendix A), are hosted by M 32, NGC 5102, NGC 4244, and NGC 7793. We note that all of them are represented by points located in the upper region of the diagrams in Figures 3 and 4. This is consistent with a dominant contribution from highly rotating and/or dynamically cooler stars formed in situ after gas inflow. In previous studies, this formation channel was in fact proposed as potentially dominant in the NSCs hosted by M 32 and NGC 5102 (e.g., Seth 2010; Nguyen et al. 2018), but it is necessary to explain observations also in NGC 4244 and NGC 7793 (e.g., Hartmann et al. 2011; Kacharov et al. 2018, see also Appendix A for the individual cases). In situ formation might therefore be the dominant mechanism in late-type NSCs and massive, rapidly rotating NSCs in early-type galaxies.

### 6.2. The Formation of Lower-angular-momentum NSCs

In the bottom-left region of Figures 3 and 4, we have three of our nuclei, hosted by early-type galaxies. The nucleus of NGC 404, represented by the lowest point in the diagrams, shows two counter-rotating structures, while the one in NGC 205 displays an offset between the rotation axis and the minor axis. In both cases, the complex kinematics suggest a formation in different episodes with one or more mergers playing a major role. As mentioned in Appendix A, these mergers would have allowed for the accretion of star clusters and/or triggered star formation bursts. On the other hand, no kinematic-decoupled components are detected in the nucleus of NGC 5206. However, we know from the photometric decomposition (Nguyen et al. 2018) that this NSC is also made up of different components: an inner one and a more extended one. This NSC shows a significant contribution from a continuous in situ star formation (Kacharov et al. 2018; see also Appendix A).

In summary, while some amount of nuclear in situ star formation might be ubiquitous for all kinds of galaxies, this mechanism seems to dominate in NSCs of late-type galaxies. On the other hand, the picture is not as clear for early-type galaxies. The latter are characterized by more complex structures and a large variety of different cases.

### 6.3. The Formation of NSCs in the Context of Their Host Galaxies

In our sample, the ubiquity of rotation, together with the signs of past interactions, are very often in conjunction with peculiar gas structures. As in Appendix A, the presence of some amount of gas was previously shown in all of our host galaxies except M 32, probably because of its dramatic past stripping processes related to its interaction with M 31 (e.g., Dierickx et al. 2014). This suggests that gas accretion might play a key role in the formation and growth of NSCs, leading either to nuclear in situ star formation or to clustered star formation in the galactic disk (outside the nucleus) followed by a migration toward the center.

Very often, the gas structures observed in our sample were associated with past interactions. The latter might be fundamental for nucleation, as they can provide not only external gas but also star clusters from the accreted satellites. In addition, they can trigger in situ star formation. Evidence for gas inflow toward the galactic center, in the shape of filaments, bars, or galactic fountains, was previously provided for four out of six late-type galaxies in our sample (M 33, NGC 2403, NGC 2976, and NGC 4449; see Appendix A and references therein). In addition, signs of very recent or ongoing in situ star formation suggest that this plays in general a major role in assembling NSCs of late-type galaxies.

The strong rotation in M 32's and NGC 5102's nuclei, the two points associated with early-type galaxies that are located in the upper region of the  $(V/\sigma)_e$  and  $\lambda_{R_e}$  diagrams, may be related to the peculiar past of their hosts as spiral galaxies. M 32 is considered the stripped remnant of a more massive spiral (e.g., Dierickx et al. 2014; D'Souza & Bell 2018). NGC 5102, the most massive galaxy in our sample, is a peculiar lenticular, sharing properties with late-type galaxies, such as its extended atomic-gas component. It would have consumed most of its gas during past intense star formation and merger episodes, becoming a lenticular (e.g., Davidge 2008). These two NSCs probably kept the kinematic properties of their disky progenitors and/or they were formed via in situ star formation triggered by the interactions that led to their galaxy-type transition (see Appendix A for more details and references). To sum up, all nuclei in the upper region of Figures 3 and 4 (all hosted by late-type galaxies plus two early types) have shown in previous works signs of gas inflow and/or in situ star formation. This is in agreement with a major role of in situ formation in those nuclei that are segregated in the upper region of the  $(V/\sigma)_e$  and  $\lambda_{R_e}$  diagrams.

On the other hand, intense merger histories may lead to lower values of  $(V/\sigma)_e$  and  $\lambda_{R_e}$ , when associated with complex nuclear structures. The complexity found in the nucleus of NGC 404, the lowest point in the diagrams, extends to the large scales of the host galaxy, and is consistent with the merger NSC origin suggested by our results (Appendix A). This lenticular galaxy displays a peculiar gas structure made up of different kinematically decoupled components, while the complex stellar populations also result from the combination of different contributions (e.g., del Río et al. 2004; Bouchard et al. 2010). Similarly, the complex stellar and gas large-scale properties of NGC 205 show signs of the past interactions, mainly with M 31 (e.g., Davidge 2003a), that would have led to the observed nuclear properties (see Appendix A for more details and references). Although the nucleus of NGC 5206 does not show such complex (kinematic) properties, previous

studies have shown potential hints of past interactions (e.g., Laurikainen et al. 2010). These might have led to the formation of the NSC and its relatively low values of  $(V/\sigma)_e$  and  $\lambda_{R_e}$ .

### 6.4. The Formation of Previously Studied NSCs

We add now to this discussion the NSCs from previous publications that were presented in Section 5.3.1. Lyubenova & Tsatsi (2019) compared their kinematic results with  $N$ -body simulations from Antonini et al. (2012), Perets & Mastrobuono-Battisti (2014), and Tsatsi et al. (2017). They showed that, in general, observed rotation can be recovered with multiple mergers of GCs, in a galactic center with an initially nonrotating bulge. Most of the results from Lyubenova & Tsatsi (2019) were in agreement with models of GCs infalling isotropically from random directions. These results correspond to the open red circles in the bottom-left region of Figures 6 and 7.

However, in situ star formation from infalling gas could also be the source of rotation in FCC 47 and FCC 170, with much higher values of  $(V/\sigma)_e$  and  $\lambda_{R_e}$ . While Lyubenova & Tsatsi (2019) showed that the high nuclear angular momentum of FCC 47 could be explained with the infall of GCs from similar orbital directions to each other (as they would do if they formed in the galactic disk), a more complex origin was proposed by Fahrion et al. (2019). They invoked additional in situ star formation, with mergers playing a significant role, to explain the high rotation, metallicity, and mass ( $\sim 7 \times 10^8 M_\odot$ ) of this kinematically decoupled NSC. On the other hand, the position of FCC 170 in the  $\lambda_{R_e}$  diagram was not consistent with any of the GC-merger simulations including a bulge presented by Lyubenova & Tsatsi (2019). They suggested that alternative mechanisms involving gas led to the formation and growth of this NSC. Therefore, in situ formation would have been important in the four nuclei in early-type galaxies that are located in the upper region of Figures 6 and 7 (M 32, NGC 5102, FCC 47, and FCC 170).

The MW hosts the best-studied NSC, whose origin is nevertheless still partly unclear due to its complex nature. On the one hand, it corotates with the Galactic disk but with a kinematic misalignment, while an additional inner component rotates perpendicular to the major axis. This structure suggests different episodes of star-cluster accretion (Feldmeier et al. 2014; Feldmeier-Krause et al. 2017b). On the other hand, the stellar populations disfavor a pure star-cluster infall scenario. For example, the wide range of metallicities is consistent with a formation in different episodes and probably via different mechanisms. The more metal-poor stars might have belonged originally to GCs that migrated to the Galactic center (Feldmeier-Krause et al. 2017a, 2020).

Furthermore, a kinematically distinct metal-poor substructure has been recently identified in the central parsec, probably a remnant of a massive star cluster or an accreted dwarf (Arca Sedda et al. 2020; Do et al. 2020). However, the dominant populations, with their super-solar metallicity much higher than MW GCs, as well as a few very young stars uniformly concentrated in the center, were instead formed in situ (Feldmeier-Krause et al. 2015). A complex formation scenario, but with in situ star formation contributing most of the mass and the strong rotation, might explain the location of the MW in the uppermost region of the  $(V/\sigma)_e$  and  $\lambda_{R_e}$  diagrams.

The NSCs hosted by FCC 47 and the MW, both massive (more than  $10^7 M_\odot$ ; see Section 5.3.1 for the MW), are

represented by points close to the massive NSCs in our sample, in Figures 6 and 7. Following the discussion in Section 6.1 and in agreement with the mentioned previous studies, this supports a scenario in which a dominant role of gas inflow and in situ star formation, contributing to higher values of  $(V/\sigma)_e$  and  $\lambda_{Re}$ , is required for the growth of massive NSCs.

### 6.5. Insights from Globular Clusters and Ultra-compact Dwarfs

The bottom-left region of Figures 6 and 7 is populated by nuclei of early-type galaxies, but also by the GCs of Kamann et al. (2018). These GCs do not extend to as high ellipticities,  $(V/\sigma)_e$ , or  $\lambda_{Re}$  values as the other NSCs, indicating that on average NSCs are more rotation dominated than their GC counterparts. On average, NSCs have larger masses than GCs, but low-mass NSCs have similar masses and metallicities to GCs at the high-mass end (Fahrion et al. 2021). If larger masses are related to stronger rotation (as suggested in Sections 6.1 and 6.4), massive GCs will have similar kinematic properties to less-massive NSCs as we see in Figures 6 and 7.

Kamann et al. (2018) suggested that GCs are born with significant angular momentum, inherited from the progenitor gas, which is however dissipated over time. This is consistent with a recent study by Lahén et al. (2020), on the kinematics of simulated young massive star clusters, formed during a merger-induced starburst. They showed how some recently formed massive clusters lie in the upper region of the  $(V/\sigma)_e$  and  $\lambda_{Re}$  diagrams, where our late-type nuclei are located. Pfeffer et al. (2020) agreed that the observed properties of GCs can be the result of the evolution of (massive) star clusters, formed in the early universe initially with similar properties as present-day young clusters (see also Portegies Zwart et al. 2010). Hence, not only can NSCs form from the infall of GCs to the galactic center, but the seeds for the formation of both NSCs and GCs might also have had very similar properties.

In addition, as suggested by, e.g., Böker (2008), (some) GCs might be the nuclear remnants of dwarf satellites accreted by massive galaxies. This is another channel of the tight evolutionary connection between (some) NSCs and GCs. Some MW GCs, in fact, are thought to be stripped nuclei. This is the case, e.g., for  $\omega$ Cen (Hilker & Richtler 2000; Noyola et al. 2008; Pfeffer et al. 2021) and M 54 (Ibata et al. 2009; Alfaro-Cuello et al. 2019, 2020; Pfeffer et al. 2021), the two most massive GCs in the MW. They were not included in the sample by Kamann et al. (2018).

M 54, with available kinematics from Alfaro-Cuello et al. (2020), was added in Figures 6 and 7. M 54 is the stripped nucleus of the disrupted Sagittarius dwarf spheroidal galaxy, as supported by its complex stellar populations (Bellazzini et al. 2008; Mucciarelli et al. 2017; Alfaro-Cuello et al. 2019). It lies as well in the bottom-left region of the diagrams. As shown by Alfaro-Cuello et al. (2019, 2020), its integrated kinematics is the result of the combination of three main stellar populations: an old and metal-poor component with a very low amount of rotation, an intermediate-age metal-rich component with some rotation, and a young, rapidly rotating, metal-rich population. While properties of the young component pointed to an in situ origin, GC accretion was proposed for the old populations. M 54 is one more example, in the bottom region of the  $(V/\sigma)_e$  or  $\lambda_{Re}$  diagrams, of a complex nuclear structure made up of components with different origin, probably the results of past interactions.

We also include two stripped nuclei into our discussion, M 59-UCD 3 and M 60-UCD 1. Their central over-massive SMBHs suggest that these UCDs are the stripped nuclei of much more massive progenitors ( $10^9$ – $10^{10} M_\odot$ ; Seth et al. 2014; Ahn et al. 2018). The latter hosted NSCs, which are now observed as the inner morphological components of these UCDs (see also Pfeffer & Baumgardt 2013). Nevertheless, nothing can be said about the morphological type of these progenitors. These stripped nuclei are located, in Figures 6 and 7, in the bottom-left region characterized by GCs and nuclei in early-type galaxies, very close to NGC 205’s nucleus. Both show strong rotation and high velocity dispersion (with a central peak associated with the SMBH). M 59-UCD 3 displays a complex structure with multiple stellar populations (Ahn et al. 2018), similarly to other early-type galaxies in our sample (Section 6.3). M 60-UCD 1 seems to be populated mainly by uniformly old stars, suggesting that it was stripped a long time ago, preventing any recent in situ growth (Seth et al. 2014). However, the amount of rotation observed in the inner region of these peculiar objects ( $\sim 40 \text{ km s}^{-1}$ ; Seth et al. 2014; Ahn et al. 2018) is much larger than that observed in most early-type nuclei in our sample. It is instead comparable to those located in the upper region of the  $(V/\sigma)_e$  or  $\lambda_{Re}$  diagrams.

## 7. Conclusions

We used a unique data set, from AO-assisted IFS in the CO band-head, of the nuclear regions of 11 early- and late-type galaxies. From these data cubes, we extracted and analyzed their resolved kinematics, at a parsec or subparsec scale. We provided the high-resolution maps of the first four moments of the LOSVD and their uncertainties, indicating that some level of rotation is ubiquitous in NSCs. The maps extracted from the highest-S/N data cubes show some kinematic complexity.

We analyzed the balance of ordered rotation and random motions in our targets, making use of the  $(V/\sigma)_e$  and  $\lambda_{Re} - \epsilon_e$  diagrams. Nuclei hosted by late-type galaxies are located in the upper, rotation-dominated region of the diagrams. On the other hand, early-type nuclei display a larger variety of cases corresponding to different locations in the diagrams. They show, on average, lower amounts of rotation and lower ellipticity, very often associated with complex kinematic structures. However, some peculiar early-type galaxies host massive, strongly rotating nuclei located in the region of the diagrams dominated by late types. Therefore, nuclei hosted by late-type galaxies and massive nuclei in early types populate the upper region of the  $(V/\sigma)_e$  and  $\lambda_{Re} - \epsilon_e$  diagrams.

If rotation is associated with in situ formation from gas accretion (or the infall of coplanar star clusters) and pressure support to the merging of star clusters (in general from random directions), the continuous distribution of our points in the  $(V/\sigma)_e$  and  $\lambda_{Re} - \epsilon_e$  diagrams supports complex formation pictures driven by a mix of these scenarios. Since the highest values of  $(V/\sigma)_e$  and  $\lambda_{Re}$  correspond to nuclei in late-type galaxies and massive nuclei in early types, we suggest that in situ formation is the dominant NSC formation mechanism in late-type galaxies, but is also required for the growth of massive NSCs in galaxies of all types. This picture is supported by additional samples from previous studies.

The discussion of the properties of the individual nuclei in the context of their hosts supports our conclusions. It suggests that, in general, galaxy interactions (often triggering gas inflow and star formation bursts, but also contributing complex

structures) play a fundamental role in NSC formation. The variety of nuclear-kinematic properties in early-type galaxies is probably closely connected to the specific evolution history of their hosts, which can therefore form their NSCs in quite different ways.

Our work provides a first glimpse into the internal kinematics of a sample of NSCs, suggests that rotation is ubiquitous and provides information on the balance between the two most invoked formation scenarios proposed for NSCs. However, the variety of specific cases, complex structures, and peculiar galaxy-evolution histories make it challenging to reconstruct NSC formation only by kinematic results. Spatially resolved stellar-population properties, including star formation histories, would be necessary to better understand the complexity of these NSCs. Moreover, connecting the kinematics to detailed information on the formation mechanism is limited by seeing, projection effects, and the contributions of the underlying galaxies. Detailed modeling of these data including these effects more fully has the potential to yield better understanding of NSC formation mechanisms.

We would like to thank Anais Gonneau for her advice on the use of the XSL and Jesús Falcón-Barroso for the useful technical discussions. The authors extend a special thanks to Anja Feldmeier, Mariya Lyubenova, and Mayte Alfaro-Cuello for kindly providing the tables of their published results cited here. We also thank the anonymous referee for the valuable comments.

*Facilities:* Gemini:Gillett (NIFS/ALTAIR), VLT:Yepun (SINFONI/AO).

*Software:* Gemini IRAF Package v1.9 (<https://www.gemini.edu/observing/phase-iii/understanding-and-processing-data/data-processing-software/gemini-iraf-general>); IRAF (Tody 1986, 1993); PampelMuse (Kamann 2013); ESO SINFONI pipeline (Eisenhauer et al. 2003; Freudling et al. 2013); VorBin (Cappellari & Copin 2003); pPXF (Cappellari & Emsellem 2004; Cappellari 2017); MgeFit (Emsellem et al. 1994; Cappellari 2002); astropy (Astropy Collaboration et al. 2013, 2018); photutils (Bradley et al. 2020).

## Appendix A Individual Nuclei: Their Host Galaxies and Kinematic Maps

In this Appendix, we describe briefly the host galaxies in our sample, giving potentially relevant information for the formation of their NSCs, and we show individual nuclear-kinematic maps extracted from our observations. In the top row of Figure Set 8, we show the first four moments of the LOSVD. From left to right: mean velocity  $V$ , velocity dispersion  $\sigma$ , skewness  $h_3$ , and kurtosis  $h_4$ .  $V$  (top-left panel) was corrected for an approximation of the systemic velocity, calculated as the average value within the central  $0''.3 \times 0''.3$ . In the bottom row, we show the respective uncertainties, per Voronoi bin, of the first four moments of the LOSVD. The dashed green ellipses indicate the  $R_{e,NSC}$  elliptical isophotes. For completeness and to avoid a subjective selection, we show the full Voronoi-binned area, although numerous bins display large uncertainties. These give often a qualitative idea of the kinematic trend in the outer region of the nuclei. Similar kinematic maps of M 32, NGC 205, NGC 404, NGC 5102, and NGC 5206 were already published (Seth et al. 2008, 2010; Seth 2010; Nguyen et al. 2018). However,  $h_3$  and  $h_4$  were not included for all of them and, when possible, we cover a wider area. For these reasons

and for completeness, we show here the maps of our full sample, consistent with the previously published ones.

### A.1. Early-type Galaxies

Of the 11 host galaxies in our sample, five are classified as early types (Table 1). We describe and discuss briefly each one of them and the kinematics of their nuclei as follows.

#### A.1.1. M 32

M 32 is a dwarf compact elliptical (cE) in the Local Group, close satellite of M 31. It hosts the least massive of the three SMBHs detected in the Local Group ( $\sim 2.4 \times 10^6 M_\odot$ ; e.g., Verolme et al. 2002; Seth 2010; van den Bosch & de Zeeuw 2010; Nguyen et al. 2018). M 32's origin is still controversial. As also suggested by its SMBH, it is thought to be a tidally stripped remnant, resulting from the interaction with its massive neighbor M 31 (e.g., Dierickx et al. 2014; D'Souza & Bell 2018). One possibility is that its progenitor was a low-luminosity spiral (Bekki et al. 2001). In support of this “threshed-spiral” scenario, a faint stellar disk was identified by Graham (2002) and Nguyen et al. (2018) in the outer parts of M 32. Furthermore, stellar kinematics of M 32 from Verolme et al. (2002) and Dressler & Richstone (1988) show disklike rotation with a maximum velocity of  $\sim 60 \text{ km s}^{-1}$ , slightly decreasing toward the outskirts. Two main stellar populations were identified in M 32. One older than 5 Gyr with subsolar metallicities, the other younger and metal-rich (Schiavon et al. 2004; Monachesi et al. 2012), contributing mostly in the nuclear region (Rose et al. 2005; Coelho et al. 2009; Miner et al. 2011).

The high S/N per spaxel allows us to observe kinematic features in M 32's nucleus at subparsec resolution in the full FOV, as shown in Figure 8. We find evidence of a relatively rapidly rotating disklike component, with velocities up to  $\sim 60 \text{ km s}^{-1}$  (top-left panel) that are clearly anticorrelated with skewness (third top panel from the left). This anticorrelation suggests disklike rotation superimposed on weaker or no rotation (e.g., van der Marel & Franx 1993). Velocity dispersion displays a strong peak in the center, which can be explained by the presence of an SMBH. A structure of higher values of  $\sigma$  appears to be aligned with the minor axis. The kurtosis map, anticorrelated with  $\sigma$ , shows slightly negative values, indicating broader profiles of the LOSVD with respect to a Gaussian, along the rotation axis and positive values across the rest of the disk. As discussed by Seth (2010), these  $h_3$  and  $h_4$  maps suggest the superposition in the LOS of a dominant rotating disk on a much slower or nonrotating bulge.

Due to the proximity of this galaxy, small structures in the eight maps might correspond to individual stars, deviating from the integrated kinematics of the galaxy and determining larger uncertainties. The high quality of this data allows us to determine the kinematic parameters with low uncertainties: generally below  $2 \text{ km s}^{-1}$  for  $V$  and  $\sigma$  and below 0.02 for  $h_3$  and  $h_4$ . Uncertainties are higher close to the edges of the FOV. Kinematic maps in Seth (2010) are within our uncertainties. Our results are also compatible with other previous studies (Dressler & Richstone 1988; Joseph et al. 2001).

The strong disklike rotation in the massive nucleus of M 32 ( $\sim 10^7 M_\odot$ ; see Nguyen et al. 2018), typical of the central regions of disky elliptical galaxies, is consistent with an in situ formation from accreted gas (Joseph et al. 2001; Hoffman et al. 2009; Seth 2010). Nuclear kinematics can be related to M 32's controversial origin. In Figures 3 and 4, the nucleus of M 32 lies in the uppermost region covered by late-type galaxies and shows one of the highest

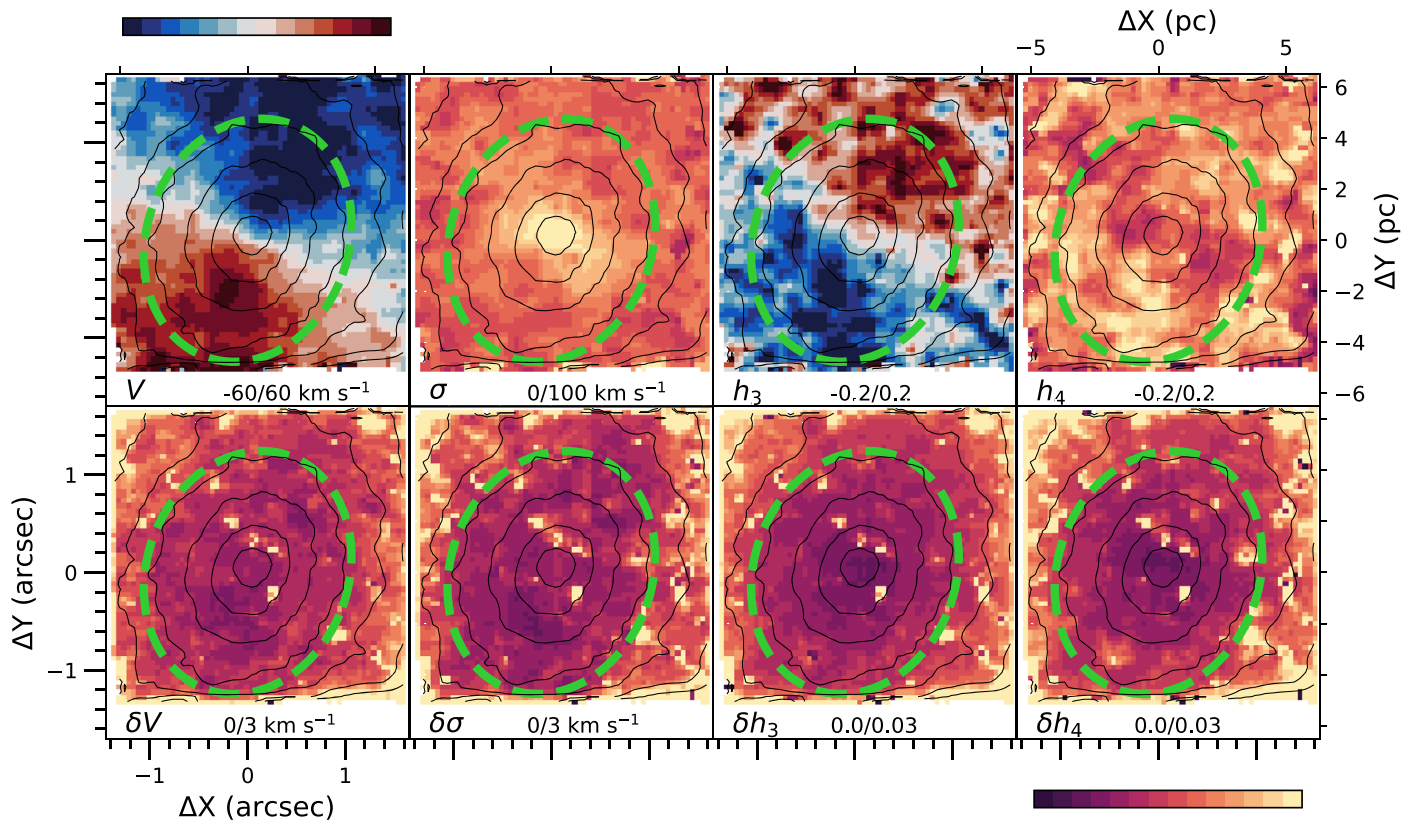


**Figure 8.** For the nuclear region of M 32, maps of the first four moments of the LOSVD, in the top row. From left to right, as indicated on the bottom left of each panel: mean velocity  $V$ , velocity dispersion  $\sigma$ , skewness  $h_3$ , and kurtosis  $h_4$ . Their respective uncertainties are shown in the bottom row. The color bar shown in the top-left panel was used for  $V$  and  $h_3$ , while the one indicated in bottom right panel was used for  $\sigma$ ,  $h_4$ , and all uncertainties. The maximum and minimum values of the color bars for each map are indicated at the bottom of each panel. The original data cube was Voronoi-binned to an S/N of 25 per bin. Different isophotes are plotted in black to guide the eye. The dashed green ellipse corresponds to the  $R_{e,NSC}$  elliptical isophote.

(The complete figure set (11 images) is available.)

proportions between ordered and random motions, in spite of the high values of velocity dispersion. If the compact galaxy that we see today is a tidally stripped remnant, the nucleus might be still bearing the footprint of its “threshed”-spiral host. It corotates with the galaxy, as can be seen from comparison with the larger-scale kinematics mapped by Verolme et al. (2002), while its chemical properties, consistent with a spiral and not with a classical elliptical galaxy, also point to this same scenario (Davidge et al. 2008). Strong tidal interactions with M 31 may have also favored gas inflow toward the center, ending in a starburst, forming the youngest populations in the NSC (Bekki et al. 2001).

#### A.1.2. NGC 205

NGC 205 is also located in the Local Group and is the brightest and the closest to M 31 of its three dwarf-elliptical (dE) companions (Davidge 2005). Several signs of past interactions with M 31 have been found in both stellar and gas properties of NGC 205 (e.g., Cepa & Beckman 1988; Young & Lo 1997; Mateo 1998; Davidge 2003a; McConnachie et al. 2004; Thilker et al. 2004). NGC 205 was initially thought to be an old galaxy (globally), since its stellar populations were associated with the ones in MW GCs (Mould et al. 1984; Baade 1944). However, signs of recent star formation activity, probably triggered by interactions with M 31, were later found in the central regions (Mateo 1998; Cappellari et al. 1999; Davidge 2003a; Butler & Martínez-Delgado 2005).

We observe relatively slow rotation in the nucleus of NGC 205. The rotation does not happen around the photometric minor axis, as seen in the top-left panel of Element 2 in Figure 8, suggesting that mergers played an important role in the formation of this NSC. Velocity dispersion drops in the central region within the  $R_{e,NSC}$  elliptical isophote, which is in agreement with the presence of a low-mass central BH as first investigated by Valluri et al. (2005) and Nguyen et al. (2018). Nguyen et al. (2019) provided a model of the measured kinematics and measured the BH mass ( $\gtrsim 5 \times 10^3 M_\odot$ ). The low  $\sigma$  values are also consistent with the observed dominant young dynamically cold populations (De Rijcke et al. 2006).

We consider the absolute values of  $V$  and  $\sigma$  to be reliable only within the  $0''.5$ – $0''.7$  isophotes, where uncertainties are not too large. However, a larger portion of the FOV hints that the galaxy may follow a similar rotation pattern and a velocity dispersion increasing farther from the center. Significant rotation was measured at larger scales, but along the major axis of the galaxy (Simien & Prugniel 2002). No pattern can be distinguished in our  $h_3$  and  $h_4$  maps, in general with large uncertainties. Our results are consistent with the kinematic maps published by Nguyen et al. (2018).

The nucleus of NGC 205 is located, in Figures 3 and 4, in the bottom-left region dominated by nuclei in early-type galaxies. Although this might be partially due to the impact of the PSF (see Appendix D), we suggest that it is also related to the complex structure suggested by both the kinematics and the



stellar populations that were found in this blue NSC, whose total mass is  $\sim 2 \times 10^6 M_\odot$  (De Rijcke et al. 2006). Young stellar populations ( $< 1$  Gyr old) dominate, while they coexist with intermediate-age stars (Bica et al. 1990; Butler & Martínez-Delgado 2005; Monaco et al. 2009; Nguyen et al. 2019), suggesting that this NSC was formed in different episodes, and different mechanisms might have been at play. Its rotation decoupled from its larger-scale host points to a significant merger contribution for its stars or the gas generating them.

### A.1.3. NGC 404

NGC 404 is a nearly face-on dwarf lenticular galaxy ( $\sim 11^\circ$  inclined; del Río et al. 2004), hosting a low-ionization nuclear emission-line region (Ho et al. 1997; Boehle et al. 2018; Dumont et al. 2020), powered by a BH of  $\sim 5.5 \times 10^5 M_\odot$  (Davis et al. 2020). As a member of the galaxy group LGG 11, it is relatively isolated (Garcia 1993; Williams et al. 2010a). NGC 404 is characterized by a prominent warped HI component, something rather exceptional for an early-type galaxy. An extended gaseous disk with a doughnut shape, with the optical galaxy located within the hole, is combined with a misaligned and kinematically decoupled more elliptical annulus (del Río et al. 2004).

A merger origin was proposed for this complex structure, with recent star formation associated with a rejuvenating process (see also Bouchard et al. 2010; Thilker et al. 2010; Williams et al. 2010a). The properties in the central region of this galaxy, with a massive gas and dust cloud and younger stellar populations than in the disk, support this scenario and suggest star formation in different episodes (Wiklund & Henkel 1990; Tikhonov et al. 2003; Cid Fernandes et al. 2005; Bouchard et al. 2010; Seth et al. 2010; Williams et al. 2010a). The complex stellar structure of NGC 404 may be the result of the combination of in situ older components with newer ones acquired during mergers. These may have taken the galaxy through a morphological transition from spiral to lenticular (Bouchard et al. 2010).

The kinematics of NGC 404's nucleus is shown in Figure 8 (Element 3). We obtained good  $V$  and  $\sigma$  maps in a large portion of the FOV, recovering the same structures and values (within our errors) as published by Seth et al. (2010). We add here  $h_3$  and  $h_4$ , with low uncertainties only within the  $R_{e,\text{NSC}}$  elliptical isophote. Kinematics reveals a complex structure. Out of the  $R_{e,\text{NSC}}$  ellipse, we observe a disklike rotating structure, as also suggested by the  $V-h_3$  anticorrelation. This component is kinematically decoupled from the close surroundings, but corotating with the HI disk (del Río et al. 2004; Bouchard et al. 2010; Seth et al. 2010). The region within the  $R_{e,\text{NSC}}$  rotates slower and/or the lower measured  $V$  might be due to the additional counter-rotating structure that is seen in the center of our  $V$  map. This was already identified by Seth et al. (2010) within the central  $\sim 0''.2$  and associated with a distinct photometric component and the detection of hot dust. A higher  $\sigma$  within the  $R_{e,\text{NSC}}$  than in the surroundings is observed. The central values are in agreement with those of Ho et al. (2009).

The presence of the inner counter-rotating component superposed to the outer one leads to a lower integrated rotation velocity and a higher dispersion in the LOS. In fact, NGC 404 is the lowest and leftmost point in the diagrams in Figures 3 and 4. While its location is probably affected by different factors such as the low inclination, the contamination of the

underlying galaxy, and the mass of the central BH, it might be mainly due to the presence of kinematically distinct components in the LOS (see also Section 5.2).

A dominant stellar age of  $\sim 1$  Gyr and some other younger and older populations suggest the formation of this NSC during bursts of star formation triggered by gas inflow during mergers (Cid Fernandes et al. 2005; Bouchard et al. 2010; Seth et al. 2010). Nguyen et al. (2017) suggested that the 1 Gyr population is most dominant in the central  $\sim 0''.2$ , indicating that the counter-rotating component was formed at that time, probably in situ after a minor merger, as suggested by its compactness. NIR emission lines in this nucleus also revealed gas thermal excitation from shocks (Seth et al. 2010; Boehle et al. 2018). The complex gas structure of the galaxy also points to the merger scenario. In conclusion, the position of this nucleus in the  $(V/\sigma)_e$  and  $\lambda_{\text{Re}}$  diagrams might be indicating a complex NSC formation, led by past mergers either via star-cluster accretion or in situ starbursts after gas inflow.

### A.1.4. NGC 5102

NGC 5102 is located in the Cen A group, and it is classified as an S0, although some of its properties are not typical of an early-type galaxy (e.g., Davidge 2008). For instance, it is bluer than a typical S0, and it has an extended HI disk (van Woerden et al. 1993). Davidge (2008) defined it as a post-starburst galaxy because of the signs of past large-scale star formation, and he suggested that it could have been a late-type spiral in the past. Integral-field spectroscopy data from Multi-Unit Spectroscopic Explorer (MUSE; Mitzkus et al. 2017), covering up to the galaxy effective radius, revealed two counter-rotating disks, one more centrally concentrated than the other. Mitzkus et al. (2017) argued that the more extended disk had been formed already, when counter-rotating gas was accreted and formed the second disk (see also van Woerden et al. 1993). Stellar-population analysis shows a strong gradient in both age and metallicity, with younger and more metal-rich stars toward the center. X-ray emission was detected by Kraft et al. (2005) both as a point source in the center probably indicating a low-luminosity active galactic nucleus, and a diffuse emission, in the central kiloparsec, probably due to hot gas shocked during the most recent starburst. An SMBH ( $M_{\text{BH}} \sim 9 \times 10^5 M_\odot$ ) was detected by Nguyen et al. (2018, 2019).

This NSC was photometrically fitted by Nguyen et al. (2018) with two Sérsic components. One of them is more massive, flatter, and more extended (with  $R_{e,\text{NSC}} \sim 32$  pc) than the inner younger one (with  $R_{e,\text{NSC}} \sim 1.6$  pc). Only some of the outer component was covered by the SINFONI FOV. In Element 4 of Figure 8, we indicate with a green dashed ellipse the area where we integrated  $(V/\sigma)_e$  and  $\lambda_{\text{Re}}$  (see Section 4.5). The region in our FOV displays relatively strong rotation, with maximum values at almost  $40 \text{ km s}^{-1}$  (top-left panel). This rotation corresponds to the outer Sérsic component. Nguyen et al. (2018) suggested that both components may have been formed in situ, in different episodes, from gas inflow related to mergers. Davidge (2015), Mitzkus et al. (2017), and Kacharov et al. (2018) measured ages of  $\lesssim 1$  Gyr in the NSC, much younger and more metal-poor than the surrounding galaxy. The nuclear outer component corotates with the larger-scale inner disk found by Mitzkus et al. (2017), and both counter-rotate with respect to the outer galaxy. Therefore, both may have formed from the same gas-accretion processes.

The very central region is associated with a peak in velocity dispersion up to  $\sim 60 \text{ km s}^{-1}$  (second top panel from left), consistent with the presence of an SMBH.  $h_3$  and  $h_4$  are anticorrelated, respectively, with  $V$  and  $\sigma$ , although their values show large relative uncertainties. This NSC appears to be more massive than the average for galaxies with similar stellar mass or velocity dispersion, with an NSC stellar mass of  $\sim 7 \times 10^7 M_\odot$  (Nguyen et al. 2018). Like the massive one in M 32, it lies in the upper region of the  $(V/\sigma)_e$  and  $\lambda_{R_e}$  diagrams (Figures 3 and 4), more typical of late-type hosts. Both galaxies may show, in their nuclear kinematics, hints of their past as spirals and of the interactions that led to their transformation to early types.

#### A.1.5. NGC 5206

NGC 5206 is another nucleated S0 galaxy in the Cen A group. Not much is found in the literature about this galaxy's past. However, the following complex structure may be the signature of past interactions. Apart from the bright nucleus (Caldwell & Bothun 1987), its brightness profile may indicate the presence of a bulge-like component, with a bulge-to-total flux ratio of 0.08, closer to values of typical spiral galaxies (Laurikainen et al. 2010). Moreover, Laurikainen et al. (2010) described a “very faint dispersed bar” (at radii lower than 1.4 kpc) and a faint lenslike structure at radii lower than 0.3 kpc. In contrast, Nguyen et al. (2018) fitted HST images with only one (disk) component apart from the NSC. They observed a color gradient toward bluer stars in the center. Some ionized gas was detected in this galaxy (Cote et al. 1997; Kennicutt et al. 2008), and a poor atomic-gas fraction (lower than 0.1%) was calculated by de Swardt et al. (2010). Nguyen et al. (2018, 2019) detected an SMBH of  $M_{\text{BH}} \sim 5\text{--}6 \times 10^5 M_\odot$ .

Nuclear kinematic maps of NGC 5206 (Figure 8, Element 5) are characterized by slow rotation and higher velocity dispersions in the very central region, closer to the SMBH. Nguyen et al. (2018) presented kinematic maps in a smaller central region, with results consistent with ours. No structures can be identified in our maps of  $h_3$  and  $h_4$ . As in NGC 5102, the brightness profile of the NSC was fitted with a double Sérsic (Nguyen et al. 2018). However, in this case, the two components have similar morphologic and kinematic properties. Kacharov et al. (2018) analyzed the stellar populations of this NSC and proposed a continuous star formation and gradual chemical enrichment. Most NSC stars would have been formed less than 4.5 Gyr ago, with a peak  $\sim 2$  Gyr ago. No substantial difference in age and metallicity was found with respect to the surrounding field stars of the galaxy. In Figures 3 and 4, NGC 5206 is located in the bottom-left region but close to the “late-type dominated region,” as well as NGC 205. In both galaxies, this might be related to the composition of different stellar populations with different kinematic signatures.

### A.2. Late-type Galaxies

Six host galaxies of our 11 nuclei are classified as late types (Table 1). Host galaxies and nuclear kinematics are individually described and briefly discussed as follows.

#### A.2.1. M 33

M 33 is a late-type spiral in the Local Group, thought to be orbiting around M 31 (e.g., van der Marel & Guhathakurta 2008). Weak tidal interactions with M 31 were proposed to explain

different atomic and ionized-gas structures, such as extended disk warps, an arc, and a filament (e.g., Corbelli et al. 1989; Corbelli & Schneider 1997; Putman et al. 2009; Corbelli et al. 2014; Semczuk et al. 2018; Tachihara et al. 2018). The gas in these features, coming from a galactic fountain and/or being previously stripped from M 33's disk in a previous interaction, is now falling back, fueling the intense ongoing star formation (Putman et al. 2009; Zheng et al. 2017).

With no observed bulge, a halo component and a kinematically distinct stellar stream were detected by McConachie et al. (2006). The galaxy disk shows stellar-population gradients that are consistent with an inside-out formation scenario (Beasley et al. 2015; Mostoghiu et al. 2018). However, these gradients are inverted outside the star-forming disk, suggesting a different (outside-in or ex situ) origin (see also Davidge 2003b and Robles-Valdez et al. 2013). No signatures were found of any SMBH in M 33 (e.g., Gebhardt et al. 2001). However, it hosts a bright X-ray and radio source at its center (Long et al. 1981; White et al. 2019), and it has been debated whether this emission is associated with a central (low-mass,  $\lesssim 3000 M_\odot$ ) BH (e.g., Gebhardt et al. 2001; Merritt et al. 2001).

Maps of the kinematics of the nucleus in M 33 are shown in Figure 8 (Element 6). Very high spatial resolution is maintained in the (almost unbinned) central region of M 33's nucleus, where uncertainties are below  $5 \text{ km s}^{-1}$ . Clear rotation is shown throughout the FOV, while the velocity dispersion drops within  $R_{e,\text{NSC}}$ , with values consistent with Kormendy & McClure (1993) and Gebhardt et al. (2001). This kinematics supports the lack of a central SMBH and is compatible with a low-mass central BH. A  $V - h_3$  anticorrelation is hinted while no structures are visible in the  $h_4$  map. The subtraction of individual stars from M 33's data cube might be not perfect, which leads to some residual structures that are seen in the maps.

The nucleus of M 33, with a dynamical mass of  $\sim 10^6 M_\odot$  (Kormendy et al. 2010), was defined as very compact. It is characterized by younger stars than the surroundings and bluer colors toward its center (Kormendy & McClure 1993; Lauer et al. 1998; Carson et al. 2015). It shows an important amount of dust, compatible with one or more strong starbursts occurring in the last gigayear (Gordon et al. 1999; Davidge 2000; Long et al. 2002), probably fueled by the observed gas infall. Hartmann et al. (2011), simulating the accretion of young stellar clusters to an in-place nuclear disk, could recover the properties of the NSC in M 33 (rotation, size, and ellipticity) only when the in situ disk component still dominated in mass. They concluded that gas accretion is needed to explain NSC formation in late-type spirals.

#### A.2.2. NGC 2403

NGC 2403 is very similar to M 33 in its morphology, brightness, size, gas chemical properties, and star formation history (Garnett et al. 1997; Davidge & Courteau 2002; Davidge 2003b). The transient X-ray source detected by Yukita et al. (2007) suggests the presence of a low-mass BH, of similar properties to the one at M 33's center. Being the second brightest galaxy of the M 81 group, it is located in its outskirts (e.g., Karachentsev et al. 2002; Williams et al. 2013; Carson et al. 2015). Farther from M 81 than M 33 is from M 31 (e.g., Davidge 2003b), its higher oxygen yield than M 33 suggests that it probably did not suffer from a similar gas stripping (Garnett

et al. 1997). Nevertheless, it is approaching M 81 and has several faint dwarf satellites. A close one of them is old, metal-poor, and has no gas (Karachentsev et al. 2002, 2013; Carlin et al. 2016).

NGC 2403 has an extended and complex gas and dust structure (Guélin & Weliachew 1969; Shostak 1973; Fraternali et al. 2002b; Bendo et al. 2007). Apart from the warped HI disk, an additional component, moving toward the galactic center, was observed by Fraternali et al. (2001, 2002b). It was interpreted as the result of a galactic fountain or an active gas channel between the disk and the halo (Fraternali et al. 2002a). An additional cloud close to NGC 2403, probably stripped from a satellite, was later discovered (de Blok et al. 2014). The stellar component is distributed in a young undisturbed disk and a more extended, thicker, and fainter component, which is older and metal-poor (Davidge 2003b; Barker et al. 2012; Williams et al. 2013).

Slow rotation is seen in the central region of this low-surface-brightness nucleus that appears to be almost face-on (Element 7 of Figure 8). Its low velocity dispersion (slightly higher in the very center) is in agreement with a low-mass BH. This NSC is younger than the surrounding central region of the galaxy, as well as the one in M 33, but even bluer (Davidge & Courteau 2002). However, the absence of significant emission from ionized gas suggests that the star formation might have recently halted (Böker et al. 1999; Drissen et al. 1999). The NSC displays a larger size with longer wavelengths (Carson et al. 2015), as well as M 33, suggesting that it was formed in different star formation episodes, from gas funneled from the different structures observed around.

#### A.2.3. NGC 2976

This bulgeless galaxy is classified as an Sc peculiar, and it is located in the core of the M 81 Group (e.g., Karachentsev et al. 2002). This region is covered by a system of HI clouds, filaments, and bridges connecting galaxies, including NGC 2976, to M 81 (Appleton et al. 1981; Chynoweth et al. 2008). Past interactions of NGC 2976 within the group are further supported by other studies (Carozzi-Meyssonier 1980; Adams et al. 2012; Drzazga et al. 2016). The stellar populations are distributed in a young inner disk and in an old outer component (disk or halo; Bronkalla & Notni 1990; Bronkalla et al. 1992). Inner-disk star formation, distributed in a ringlike structure, as well as outside-in gas depletion in the outer component, were probably triggered by the group environment (see also Williams et al. 2010b). Gas would have been stripped from the halo and/or channeled toward the galaxy center. Another consequence of this might be the formation of a weak (gas-rich) bar, connecting two strong H $\alpha$ -emission spots on both sides of the galaxy and favoring a potential nuclear starburst forming the NSC (Tacconi et al. 1990; Daigle et al. 2006; Menéndez-Delmestre et al. 2007; Spekkens & Sellwood 2007; Grier et al. 2011; Adams et al. 2012; Valenzuela et al. 2014).

The kinematics of this nucleus (Element 8 in Figure 8) shows clear rotation throughout the full FOV, even in the regions where large uncertainties warn us not to trust absolute values. Due to the low S/N, especially out of the  $R_{e,\text{NSC}}$  elliptical isophote, it is challenging to distinguish any structures in the maps of the higher moments  $h_3$  and  $h_4$ . We know from photometry that this NSC displays some clumpiness and a significant flattening, as a disk oriented in the same way as the galaxy (Carson et al. 2015). The evidence provided for gas inflow toward the galactic center, with the bar playing a significant role, supports an in situ formation for this NSC. However, it may have been formed in different star formation

episodes or by different formation mechanisms, since asymmetric stellar populations were identified by Carson et al. (2015). It has a more compact bluer component to the north (with the HI structures in the northeast direction; e.g., Chynoweth et al. 2008) and a more extended and irregular redder component to the south.

#### A.2.4. NGC 4244

NGC 4244 is an edge-on late-type spiral member of the M 94 Group and probably weakly interacting with NGC 4214 (e.g., Seth et al. 2005a, 2005b; Comerón et al. 2011; Carson et al. 2015). Bulgeless, its brightest components are a prominent disk and an NSC. The disk was fitted vertically with two components, a thin disk and a thick disk, by Comerón et al. (2011). It is characterized, at increasing distances from the midplane, respectively, by young, intermediate, and old stars (Seth et al. 2005a, 2005b). These populations break all at the same radius, pointing to a past interaction that may also explain the presence of a stellar diffuse component (de Jong et al. 2007; Seth et al. 2007). NGC 4244 has a massive and thick HI disk. A warped and a flaring components, as well as other peculiar features in correspondence of star-forming regions, were observed (Olling 1996; Zschaechner et al. 2011). At a smaller scale the stellar disk warps in the opposite direction to the HI disk, and shows signs of potential tidal interactions (Comerón et al. 2011). This galaxy may host in its center a massive BH of  $\sim 10^5 M_{\odot}$  (Hartmann et al. 2011; De Lorenzi et al. 2013).

The nearly edge-on nucleus of NGC 4244 (Hartmann et al. 2011) shows the highest ratio between circular and random motions in our sample (see Figures 3 and 4), with the highest  $\epsilon_e$ . Its kinematic maps are shown in Element 9 in the online figure set version of Figure 8 and are in agreement with the ones shown by Seth et al. (2008). Values of  $\sigma$  within the central region, with reasonable uncertainties, are consistent with measurements from Ho et al. (2009). A clear rotation pattern, anticorrelated with  $h_3$ , indicates a disky structure. In fact, the nucleus of NGC 4244 is made up of a compact spheroidal component and a more extended disk, corotating with the HI disk (Seth et al. 2008; Carson et al. 2015). Multiple stellar populations were identified in this NSC, with young stars ( $\sim 100$  Myr) dominating the disk component. Old and more metal-poor stellar populations dominate above and below the midplane (Seth et al. 2006, 2008). A combined accretion of gas and star clusters from the galaxy disk was proposed for the formation of this massive NSC ( $\sim 10^7 M_{\odot}$ ), supported by results from simulations and dynamical models (Hartmann et al. 2011; De Lorenzi et al. 2013).

#### A.2.5. NGC 4449

NGC 4449 is a luminous irregular galaxy with intense recent star formation and a rich population of star clusters of all ages (Kumari et al. 2017; Whitmore et al. 2020). Numerous studies presented hints of recent interactions, such as stellar tidal streams and, on the west side of the galaxy, a star cluster with a tidal structure that could be the remnant nucleus of a disrupted dwarf galaxy (Annibali et al. 2008; Martínez-Delgado et al. 2012). Although NGC 4449 appears relatively isolated, since its only close companion (in the projected space) is DDO 125, a past interaction between the two galaxies was suggested, e.g., by Theis & Kohle (2001) and Valdez-Gutiérrez et al. (2002). This would explain the complex morphology and kinematics of the extended gas structure around NGC 4449 (Bajaja et al.

1994; Hunter 1997; Hunter & Gallagher 1997). Pointing to the same direction, counter-rotation has been observed in the inner gas component (within  $\sim 4$  kpc) with respect to the outer gas envelope (Hunter et al. 1998).

In Element 10 of Figure 8, we observe slow rotation and low values of  $\sigma$ . The kinematic analysis of this nucleus was the most challenging in our sample, due to the combination of the lowest S/N among our data cubes and the low absolute values of the kinematic parameters (proving the limits of our method). The nucleus of NGC 4449, associated with intense emission of ionized gas, shows no evidence of old populations and hosts the youngest stars of the galaxy ( $\sim 10$  Myr old; Böker et al. 1999; Gelatt et al. 2001; Annibali et al. 2008). The latter indicate a very recent starburst, probably a consequence of a violent event that doubled the star formation rate between 10 and 16 Myr ago (Cignoni et al. 2018; Whitmore et al. 2020).

The relatively low metallicity shows that these stars were formed from gas that was not significantly enriched (Böker et al. 2001). This is also confirmed by the lower metallicity of ionized gas in the central region than in the rest, suggesting metal-poor gas accretion during a potential recent merger (Kumari et al. 2017). This gas might have been funneled toward the galactic center by the S-shaped structure that was observed in this nuclear region (Gelatt et al. 2001). This might be bar-like debris of a past interaction, probably a small (accreted) spiral seen edge-on. This structure (9.5 pc long; Gelatt et al. 2001), might be the rotating structure in the center of our FOV.

As it looks like a good candidate for a pure gas-accretion NSC formation, we would have expected to find this nucleus in an upper location in Figures 3 and 4. Its peculiar nature (and of its host), and the potential composition of different structures in the LOS as a result of mergers, might explain why it is the lowest point for late-type galaxies in our diagrams. Alternatively, its very young age and mass lower than  $10^7 M_\odot$  (Georgiev et al. 2016) might imply that it did not have time to grow enough and reach the high rotation levels typical of the most massive NSCs such as M 32, NGC 4244, NGC 5102, and NGC 7793.

#### A.2.6. NGC 7793

NGC 7793 is a bright spiral galaxy member of the Sculptor group. It has two dwarf close companions in the same subgroup

(Karachentsev et al. 2003). Considered as the prototype of Sd galaxies (Shapley 1943), it has no bulge (but a bright nucleus). It is rich in star-forming regions in its multiple fragmented and clumpy spiral arms (de Vaucouleurs & Davoust 1980; Smith et al. 1984; Sacchi et al. 2019). Both the extended HI and diffuse H $\alpha$  components show a declining rotation curve, some level of noncircular motions, and a warp in the outskirts (Davoust & de Vaucouleurs 1980; de Vaucouleurs & Davoust 1980; Carignan & Puche 1990; Dicaire et al. 2008). The stellar disk of NGC 7793 is made up of an old underlying component and young populations in the spiral arms (de Vaucouleurs & Davoust 1980; Davidge 1998). Old stars, with an upturn in their brightness profile in the outskirts, extend farther than the young populations and farther than the HI disk. Radial migration was proposed by Radburn-Smith et al. (2012) to explain this. The resolved star formation history of NGC 7793 reveals an increase in the star formation rate in time and spatially from the inner to the outer regions, pointing to an inside-out growth of the disk (Sacchi et al. 2019). A massive BH of  $\lesssim 5 \times 10^5$  was recently estimated by Neumayer et al. (in preparation).

The NSC in NGC 7793 is rather massive ( $7.8 \times 10^7 M_\odot$ ; Walcher et al. 2005). It shows clear rotation around its minor axis, with a slightly asymmetric pattern (Figure 8, Element 11). Velocity dispersion assumes slightly higher values in the very central region, which are in agreement with the average velocity dispersion from Walcher et al. (2005;  $\sim 24.6 \text{ km s}^{-1}$ ), measured over a  $10''$  long slit. It is difficult to distinguish any structures in the  $h_3$  and  $h_4$  maps, with high relative uncertainties. NGC 7793's nucleus, dominated by very young stars, is one of the many star formation regions in this galaxy (Diaz et al. 1982; Shields & Filippenko 1992; Walcher et al. 2006; Kacharov et al. 2018). A color gradient and a UV-prominent ring structure showed that the youngest stars are mainly located in the outer part of the NSC, suggesting circumnuclear star formation (Carson et al. 2015). The position of this nucleus in the  $(V/\sigma)_e$  and  $\lambda_{Re}$  diagrams (Figures 6 and 7), in the upper region, suggests in situ formation as the dominant formation mechanism. On the other hand, results on the stellar-population properties of this NSC, consisting of a variety of ages and metallicities, point toward multiple star-cluster mergers contributing the older components (Kacharov et al. 2018).

### Appendix B

#### $|V|/\sigma$ Radial Distribution in the Nuclear Regions of the 11 Early- and Late-type Galaxies in Our Sample

We show in Figure 9 the radial profiles of  $|V|/\sigma$  for each nucleus in our sample. Each point corresponds to  $V$  and  $\sigma$  in each

Voronoi bin, as mapped in Figure 8. Points and names of early-type galaxies are plotted in red, and those of late-type galaxies are plotted in blue. Error bars, plotted in gray, correspond to the uncertainties mapped in Figures 8. These plots may help the assessment and interpretation of Figures 3, 4, 6, and 7.

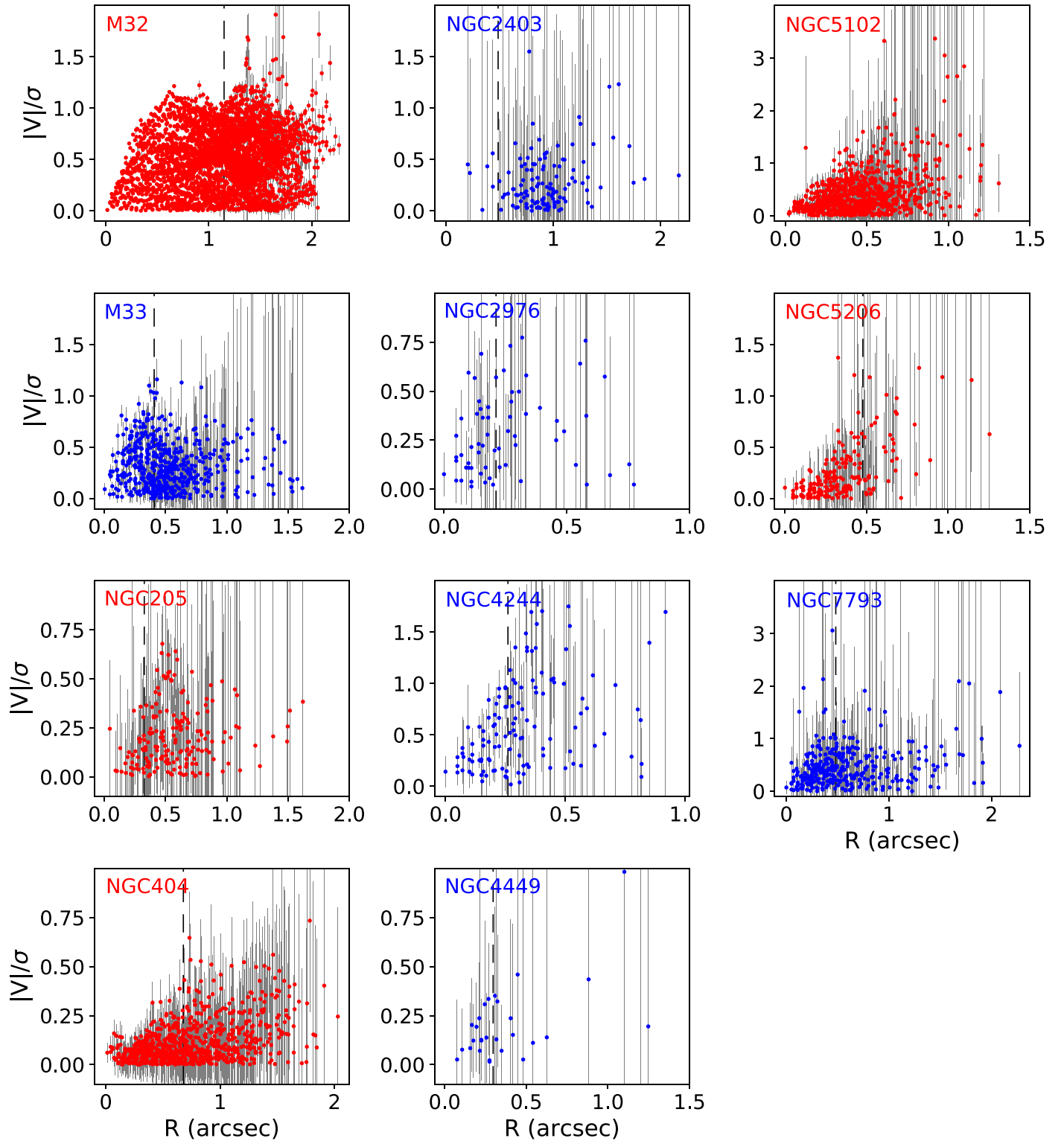


**Figure 9.** Radial distributions of  $|V|/\sigma$  in the nuclear regions of the 11 galaxies in our sample, each one in one panel. Each point corresponds to a Voronoi bin. Points in early-type galaxies are plotted in red, and those in late-type galaxies are plotted in blue. Galaxy names are indicated in the top left of each panel with the same color scheme. Error bars are plotted in gray. The horizontal axes correspond to the projected radius in the FOV, as it is observed in our NIFS and SINFONI data.  $R_{e,NSC}$  is indicated by a vertical dashed line in each panel.

### Appendix C Measurements of $\epsilon_e$ , $(V/\sigma)_e$ , and $\lambda_{Re}$ for Our Sample of 11 Nuclei

We provide in Table 2 our results for  $\epsilon_e$ ,  $(V/\sigma)_e$  and  $\lambda_{Re}$ , calculated as explained in Section 4.5, for the 11 nuclei in our

sample. These values are plotted in Figures 3, 4, 6, and 7. Values corrected from the PSF effect were calculated as explained in Appendix D and are shown in Figures 10 and 11.  $(V/\sigma)_e^{\text{corr}}$  and  $\lambda_{Re}^{\text{corr}}$  for NGC 4244, NGC 5102 and NGC 5206 are upper limits.

**Table 2**  
Kinematic Properties of Our Sample of 11 Galactic Nuclei

Galaxy Name	$\epsilon_e$	$\delta\epsilon_e$	$(V/\sigma)_e$	$\delta(V/\sigma)_e$	$\lambda_{Re}$	$\delta\lambda_{Re}$	$(V/\sigma)_e^{\text{corr}}$	$\lambda_{Re}^{\text{corr}}$
M 32	0.187	0.003	0.504	0.001	0.456	0.001	0.589	0.526
M 33	0.113	0.024	0.419	0.007	0.354	0.006	0.608	0.529
NGC 205	0.164	0.034	0.217	0.013	0.169	0.012	0.405	0.296
NGC 404	0.091	0.009	0.089	0.003	0.079	0.003	0.122	0.108
NGC 2403	0.042	0.018	0.294	0.041	0.254	0.020	0.420	0.362
NGC 2976	0.287	0.063	0.310	0.038	0.273	0.026	0.616	0.594
NGC 4244	0.465	0.035	0.572	0.018	0.499	0.014	<0.858	<0.677
NGC 4449	0.318	0.034	0.203	0.081	0.165	0.033	0.357	0.275
NGC 5102	0.243	0.004	0.325	0.007	0.351	0.005	<0.440	<0.465
NGC 5206	0.079	0.020	0.219	0.012	0.195	0.010	<0.274	<0.243
NGC 7793	0.157	0.015	0.392	0.012	0.367	0.010	0.528	0.494

**Notes.** Columns from left to right: galaxy name, ellipticity, ellipticity error,  $(V/\sigma)_e$ , its uncertainty,  $\lambda_{Re}$ , its uncertainty, PSF corrected values of  $(V/\sigma)_e$ , and PSF corrected  $\lambda_{Re}$ . All values and their uncertainties were calculated as explained in Section 4.5 and corrected from the PSF effects as explained in Appendix D.

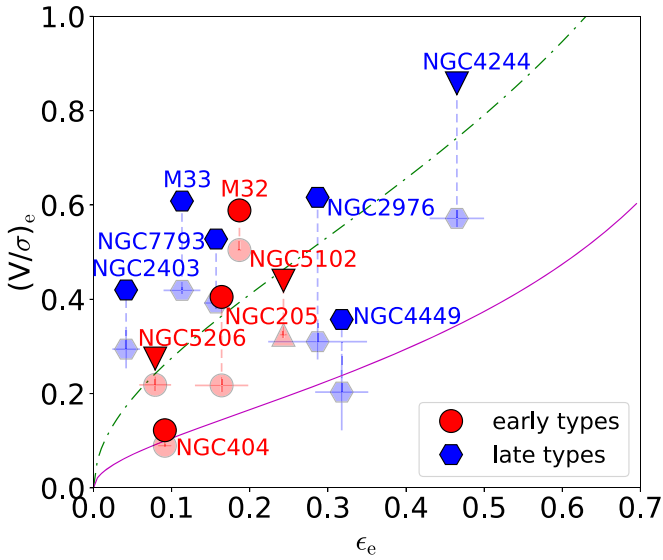


**Figure 10.** Estimate of the PSF impact on the  $(V/\sigma)_e - \epsilon_e$  diagram for the sample of 11 nuclei studied in this work. Shaded points indicate the observed  $(V/\sigma)_e$  (as in Figure 3) while filled points are the estimated values of  $(V/\sigma)_e$  after PSF correction. The names of the host galaxies are indicated close to the individual corrected points. Nuclei of early-type galaxies are plotted in red (circles or downward triangles), while those of late types are plotted in blue (hexagons or a downward triangle). Downward triangles indicate upper limits. The green dashed-dotted and the magenta solid lines are the same as in Figure 3.

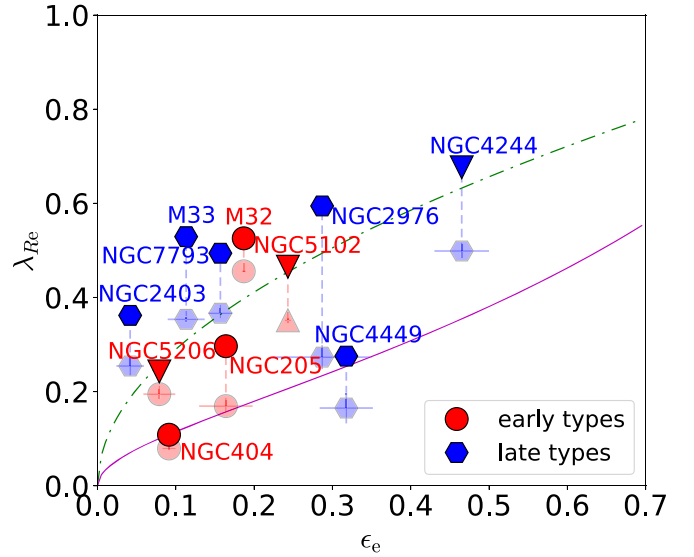


**Figure 11.** Estimate of the PSF impact on the  $\lambda_{Re} - \epsilon_e$  diagram for the sample of 11 nuclei studied in this work. Symbols, lines, and colors are the same as in Figure 10.

## Appendix D

### PSF Measurements and Their Impact on the Observed

$(V/\sigma)_e$  and  $\lambda_{R_e}$

We follow the approach of Harborne et al. (2020) to assess the impact of atmospheric seeing on our observational measurements of the nuclear  $(V/\sigma)_e$  and  $\lambda_{R_e}$ . They proposed general analytic corrections, modeled making use of mock observations of numerical simulations, accounting for the PSF effect on  $(V/\sigma)_e$  and  $\lambda_{R_e}$  on galaxies of different Hubble types. From their Equations (16), (17), and (18), the corrected  $(V/\sigma)_e$  and  $\lambda_{R_e}$  are:

$$\left(\frac{V}{\sigma}\right)_e^{\text{corr}} = 10^{\left[\log_{10}\left(\frac{V}{\sigma}\right)_e - \Delta\left(\frac{V}{\sigma}\right)_e^{\text{corr}}\right]} \quad (\text{D1})$$

and

$$\lambda_{R_e}^{\text{corr}} = 10^{\left[\log_{10}(\lambda_{R_e}) - \Delta\lambda_{R_e}^{\text{corr}}\right]} \quad (\text{D2})$$

where:

$$\Delta\lambda_{R_e}^{\text{corr}} = \left\{ \frac{7.55}{1 + \exp\left[4.42\left(\frac{\sigma_{\text{PSF}}}{R_e^{\text{maj}}}\right)^{1.55} + 2.73\right]} - 0.46 \right\} + 3\left(\frac{\sigma_{\text{PSF}}}{R_e^{\text{maj}}}\right) \times [-0.10\epsilon_e + 0.024\log_{10}(n_{\text{NSC}}) + 0.064]. \quad (\text{D3})$$

and

$$\Delta\left(\frac{V}{\sigma}\right)_e^{\text{corr}} = \left\{ \frac{7.48}{1 + \exp\left[4.08\left(\frac{\sigma_{\text{PSF}}}{R_e^{\text{maj}}}\right)^{1.60} + 2.89\right]} - 0.39 \right\} + \left(\frac{\sigma_{\text{PSF}}}{R_e^{\text{maj}}}\right) \times [0.10\epsilon_e - 0.22\log_{10}(n_{\text{NSC}}) + 0.10] \quad (\text{D4})$$

These corrections are functions of the ratio  $\sigma_{\text{PSF}}/R_e^{\text{maj}}$ , between the standard deviation of the PSF distribution  $\sigma_{\text{PSF}} = \text{FWHM}_{\text{PSF}}/(2\sqrt{2\ln 2})$ , and the major axis of the NSC half-light ellipse  $R_e^{\text{maj}}$ . In addition, the impact of the PSF depends on the concentration of the light, indicated by the Sérsic index  $n_{\text{NSC}}$ .

We show in Table 3 the details of the available PSF measurements, mentioned in Section 3, for our observations. For galaxies in Table 3, we used the light-weighted average FWHM of the different PSF-fitting components ( $\langle\text{FWHM}_{\text{PSF}}\rangle$ ). For NGC 4449, since it was not possible to derive a PSF for our data cubes from optical images (due to the complexity of its central region), we used the average PSF size measured for our observations with the same instrument and mode (NIFS with LGS AO; see Section 3.1). This corresponds to  $\text{FWHM}_{\text{PSF}} = 0''.345$ . As for  $n_{\text{NSC}}$ , we used the values in Table 1. When two values of  $n_{\text{NSC}}$  are given in the table, because the NSC was fitted with a double Sérsic profile, we

**Table 3**  
PSF Measurements for Our Observations (All Galaxies in the Sample, Except NGC 4449)







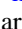



Galaxy Name	Component of the Fit	$\text{FWHM}_{\text{PSF}}$ (")	Light Fraction %	$\langle\text{FWHM}_{\text{PSF}}\rangle$ (")	Reference
M 32	Gaussian	0.23	45	0.46	Seth (2010)
	Moffat	0.66 <sup>(1)</sup>	55		
M 33	Gaussian	0.09	65	0.31	this work
	Gaussian	0.71	35		
NGC 205	Gaussian	0.25	68	0.40	Nguyen et al. (2018)
	Moffat	0.73 <sup>(1)</sup>	32		
NGC 2403	Gaussian	0.22	86	0.38	this work
	Gaussian	1.35	14		
NGC 2976	Gaussian	0.13	68	0.34	this work
	Gaussian	0.78	32		
NGC 404	Gaussian	0.12	50	0.44	Seth et al. (2010)
	Moffat	0.75 <sup>(1)</sup>	50		
NGC 4244	Gaussian	0.23	100	0.23	Seth et al. (2008)
NGC 5102	Gaussian	0.08	35	0.56	Nguyen et al. (2018)
	Gaussian	0.82	65		
NGC 5206	Gaussian	0.12	60	0.24	Nguyen et al. (2018)
	Gaussian	0.42	40		
NGC 7793	Gaussian	0.17	67	0.30	this work
	Gaussian	0.57	33		

**Note.** Two fitting components were used for most galaxies.  $\langle\text{FWHM}_{\text{PSF}}\rangle$  in the second-to-last column is the light-weighted average of the  $\text{FWHM}_{\text{PSF}}$  of the different profiles. (1) For Moffat distributions described as  $\Sigma(r) = \Sigma_0[1 + (r/r_d)^2]^{-4.765}$  (Seth 2010; Seth et al. 2010; Nguyen et al. 2018),  $\text{FWHM}_{\text{PSF}} = 2r_d\sqrt{2^{1/4.765} - 1}$  (Trujillo et al. 2001).

adopted the highest index to obtain the largest correction and to be more conservative. Therefore we obtained upper limits for the corrected values of NGC 4244, NGC 5102, and NGC 5206. Since for NGC 4449 we did not find any available value for  $n_{\text{NSC}}$ , we approximated it to the mean Sérsic index of the rest of the sample ( $n_{\text{NSC}} \sim 2.9$ ).

The obtained values of  $(\frac{V}{\sigma})_e^{\text{corr}}$  and  $\lambda_{R_e}^{\text{corr}}$  are indicated in Table 2 (Appendix C). They are shown in the  $(\frac{V}{\sigma})_e^{\text{corr}} - \epsilon_e$  and  $\lambda_{R_e}^{\text{corr}} - \epsilon_e$  diagrams plotted in Figures 10 and 11. Nuclei hosted by early- and late-type galaxies are indicated, respectively, with red circles and blue hexagons. Upper limits are indicated with downward triangles. In the figures, the corrected points are compared to the uncorrected ones from Figures 3 and 4 (shaded symbols). It is shown in Figures 10 and 11 how they move upward when the effect of the PSF is taken into account. However, each one of them does it in a different amount. While the PSF impact is relatively small for the nuclei in NGC 404 and NGC 5206, it is not so small for NGC 205. Its PSF correction, the largest among the early-type galaxies in our sample and mainly due to the small size of the NSC, drives the red circle to  $(V/\sigma)_e$  values not so different from NGC 2403 and NGC 5102. Except for NGC 205, PSF corrections are in general more significant for late-type galaxies. This is due to their stronger rotation, in some cases combined with a larger concentration of the nucleus in the center. In fact, the PSF impact is more significant for nuclei with higher  $n_{\text{NSC}}$  and  $\epsilon_e$  and with smaller  $R_{e,\text{NSC}}$  relative to the PSF size. In particular, the highest  $n_{\text{NSC}}$  determines a strong PSF effect for NGC 2976's nucleus.

### ORCID iDs

Francesca Pinna  <https://orcid.org/0000-0001-5965-3530>  
 Nadine Neumayer  <https://orcid.org/0000-0002-6922-2598>  
 Anil Seth  <https://orcid.org/0000-0003-0248-5470>  
 Eric Emsellem  <https://orcid.org/0000-0002-6155-7166>  
 Dieu D. Nguyen  <https://orcid.org/0000-0002-5678-1008>  
 Torsten Böker  <https://orcid.org/0000-0002-5666-7782>  
 Michele Cappellari  <https://orcid.org/0000-0002-1283-8420>  
 Richard M. McDermid  <https://orcid.org/0000-0002-8175-7229>  
 Karina Voggel  <https://orcid.org/0000-0001-6215-0950>  
 C. Jakob Walcher  <https://orcid.org/0000-0002-2715-796X>

### References

- Adams, J. J., Gebhardt, K., Blanc, G. A., et al. 2012, *ApJ*, 745, 92  
 Ahn, C. P., Seth, A. C., Cappellari, M., et al. 2018, *ApJ*, 858, 102  
 Alfaro-Cuello, M., Kacharov, N., Neumayer, N., et al. 2019, *ApJ*, 886, 57  
 Alfaro-Cuello, M., Kacharov, N., Neumayer, N., et al. 2020, *ApJ*, 892, 20  
 Annibaldi, F., Aloisi, A., Mack, J., et al. 2008, *AJ*, 135, 1900  
 Antonini, F., Capuzzo-Dolcetta, R., Mastrobuono-Battisti, A., & Merritt, D. 2012, *ApJ*, 750, 111  
 Appleton, P. N., Davies, R. D., & Stephenson, R. J. 1981, *MNRAS*, 195, 327  
 Arca Sedda, M., Gualandris, A., Do, T., et al. 2020, *ApJL*, 901, L29  
 Aros, F. I., Sippel, A. C., Mastrobuono-Battisti, A., et al. 2020, *MNRAS*, 499, 4646  
 Astropy Collaboration, Price-Whelan, A. M., Sipőcz, B. M., et al. 2018, *AJ*, 156, 123  
 Astropy Collaboration, Robitaille, T. P., Tollerud, E. J., et al. 2013, *A&A*, 558, A33  
 Baade, W. 1944, *ApJ*, 100, 137  
 Babcock, H. W. 1939, *LicOB*, 498, 41  
 Bajaja, E., Huchtmeier, W. K., & Klein, U. 1994, *A&A*, 285, 385  
 Barker, M. K., Ferguson, A. M. N., Irwin, M. J., Arimoto, N., & Jablonka, P. 2012, *MNRAS*, 419, 1489  
 Beasley, M. A., San Roman, I., Gallart, C., Sarajedini, A., & Aparicio, A. 2015, *MNRAS*, 451, 3400  
 Bekki, K. 2015, *ApJL*, 812, L14  
 Bekki, K., Couch, W. J., Drinkwater, M. J., & Gregg, M. D. 2001, *ApJL*, 557, L39  
 Bellazzini, M., Ibata, R. A., Chapman, S. C., et al. 2008, *AJ*, 136, 1147  
 Bender, A., Saglia, R. P., & Gerhard, O. E. 1994, *MNRAS*, 269, 785  
 Bendo, G. J., Calzetti, D., Engelbracht, C. W., et al. 2007, *MNRAS*, 380, 1313  
 Bica, E., Alloin, D., & Schmidt, A. A. 1990, *A&A*, 228, 23  
 Binney, J. 1978, *MNRAS*, 183, 501  
 Binney, J. 2005, *MNRAS*, 363, 937  
 Binney, J., & Tremaine, S. 1987, *Galactic Dynamics* (Princeton, NJ: Princeton Univ. Press)  
 Boccas, M., Rigaut, F., Bec, M., et al. 2006, *Proc. SPIE*, 6272, 62723L  
 Böker, A., Larkin, J. E., Armus, L., & Wright, S. A. 2018, *ApJ*, 866, 79  
 Böker, T. 2008, *ApJL*, 672, L111  
 Böker, T., Calzetti, D., Sparks, W., et al. 1999, *ApJS*, 124, 95  
 Böker, T., Laine, S., van der Marel, R. P., et al. 2002, *AJ*, 123, 1389  
 Böker, T., van der Marel, R. P., Mazzuca, L., et al. 2001, *AJ*, 121, 1473  
 Bonnet, H., Abuter, R., Baker, A., et al. 2004, *Msngr*, 117, 17  
 Bothun, G. D., Mould, J. R., Wirth, A., & Caldwell, N. 1985, *AJ*, 90, 697  
 Bouchard, A., Prugniel, P., Koleva, M., & Sharina, M. 2010, *A&A*, 513, A54  
 Bradley, L., Sipőcz, B., Robitaille, T., et al. 2020, *astropy/photutils*: 1.0.0, Zenodo, doi:10.5281/zenodo.4044744  
 Bronkalla, W., & Notni, P. 1990, *Astronomische Gesellschaft Abstract Series*, 5, 85  
 Bronkalla, W., Notni, P., & Mutter, A. A. R. 1992, *AN*, 313, 1  
 Butler, D. J., & Martínez-Delgado, D. 2005, *AJ*, 129, 2217  
 Caldwell, N. 1983, *AJ*, 88, 804  
 Caldwell, N., & Bothun, G. D. 1987, *AJ*, 94, 1126  
 Cappellari, M. 2002, *MNRAS*, 333, 400  
 Cappellari, M. 2016, *ARA&A*, 54, 597  
 Cappellari, M. 2017, *MNRAS*, 466, 798  
 Cappellari, M., Bertola, F., Burstein, D., et al. 1999, *ApJL*, 515, L17  
 Cappellari, M., & Copin, Y. 2003, *MNRAS*, 342, 345  
 Cappellari, M., & Emsellem, E. 2004, *PASP*, 116, 138  
 Cappellari, M., Emsellem, E., Bacon, R., et al. 2007, *MNRAS*, 379, 418  
 Capuzzo-Dolcetta, R. 1993, *ApJ*, 415, 616  
 Capuzzo-Dolcetta, R., & Mastrobuono-Battisti, A. 2009, *A&A*, 507, 183  
 Carignan, C., & Puche, D. 1990, *AJ*, 100, 394  
 Carlin, J. L., Sand, D. J., Price, P., et al. 2016, *ApJL*, 828, L5  
 Carollo, C. M., Stiavelli, M., & Mack, J. 1998, *AJ*, 116, 68  
 Carozzi-Meyssonier, N. 1980, *A&A*, 92, 189  
 Carson, D. J., Barth, A. J., Seth, A. C., et al. 2015, *AJ*, 149, 170  
 Cepa, J., & Beckman, J. E. 1988, *A&A*, 200, 21  
 Chynoweth, K. M., Langston, G. I., Yun, M. S., et al. 2008, *AJ*, 135, 1983  
 Cid Fernandes, R., González Delgado, R. M., Storch-Bergmann, T., Martins, L. P., & Schmitt, H. 2005, *MNRAS*, 356, 270  
 Cignoni, M., Sacchi, E., Aloisi, A., et al. 2018, *ApJ*, 856, 62  
 Coelho, P., Mendes de Oliveira, C., & Cid Fernandes, R. 2009, *MNRAS*, 396, 624  
 Comerón, S., Knapen, J. H., Sheth, K., et al. 2011, *ApJ*, 729, 18  
 Corbelli, E., & Schneider, S. E. 1997, *ApJ*, 479, 244  
 Corbelli, E., Schneider, S. E., & Salpeter, E. E. 1989, *AJ*, 97, 390  
 Corbelli, E., Thilker, D., Zibetti, S., Giovanardi, C., & Salucci, P. 2014, *A&A*, 572, A23  
 Côté, P., Piatek, S., Ferrarese, L., et al. 2006, *ApJS*, 165, 57  
 Cote, S., Freeman, K. C., Carignan, C., & Quinn, P. J. 1997, *AJ*, 114, 1313  
 Daigle, O., Carignan, C., Amram, P., et al. 2006, *MNRAS*, 367, 469  
 D'Souza, R., & Bell, E. F. 2018, *NatAs*, 2, 737  
 Davidge, T. J. 1998, *ApJ*, 497, 650  
 Davidge, T. J. 2000, *AJ*, 119, 748  
 Davidge, T. J. 2003a, *ApJ*, 597, 289  
 Davidge, T. J. 2003b, *AJ*, 125, 3046  
 Davidge, T. J. 2005, *AJ*, 130, 2087  
 Davidge, T. J. 2008, *AJ*, 135, 1636  
 Davidge, T. J. 2015, *ApJ*, 799, 97  
 Davidge, T. J., Beck, T. L., & McGregor, P. J. 2008, *ApJ*, 677, 238  
 Davidge, T. J., & Courteau, S. 2002, *AJ*, 123, 1438  
 Davis, T. A., Nguyen, D. D., Seth, A. C., et al. 2020, *MNRAS*, 496, 4061  
 Davoust, E., & de Vaucouleurs, G. 1980, *ApJ*, 242, 30  
 de Blok, W. J. G., Keating, K. M., Pisano, D. J., et al. 2014, *A&A*, 569, A68  
 de Blok, W. J. G., Walter, F., Brinks, E., et al. 2008, *AJ*, 136, 2648  
 de Jong, R. S., Seth, A. C., Radburn-Smith, D. J., et al. 2007, *ApJL*, 667, L49



- De Lorenzi, F., Hartmann, M., Debattista, V. P., Seth, A. C., & Gerhard, O. 2013, *MNRAS*, **429**, 2974
- De Rijcke, S., Prugniel, P., Simien, F., & Dejonghe, H. 2006, *MNRAS*, **369**, 1321
- de Swardt, B., Kraan-Korteweg, R. C., & Jerjen, H. 2010, *MNRAS*, **407**, 955
- de Vaucouleurs, G., & Davoust, E. 1980, *ApJ*, **239**, 783
- del Río, M. S., Brinks, E., & Cepa, J. 2004, *AJ*, **128**, 89
- Diaz, A. I., Pagel, B. E. J., Edmunds, M. G., & Phillips, M. M. 1982, *MNRAS*, **201**, 49P
- Dicaire, I., Carignan, C., Amram, P., et al. 2008, *AJ*, **135**, 2038
- Dierickx, M., Blecha, L., & Loeb, A. 2014, *ApJL*, **788**, L38
- Do, T., David Martinez, G., Kerzendorf, W., et al. 2020, *ApJL*, **901**, L28
- Dressler, A., & Richstone, D. O. 1988, *ApJ*, **324**, 701
- Drissen, L., Roy, J.-R., Moffat, A. F. J., & Shara, M. M. 1999, *AJ*, **117**, 1249
- Drzazga, R. T., Chyży, K. T., Heald, G. H., Elstner, D., & Gallagher, J. S. 2016, *A&A*, **589**, A12
- Dumont, A., Seth, A. C., Strader, J., et al. 2020, *ApJ*, **888**, 19
- Eisenhauer, F., Abuter, R., Bickert, K., et al. 2003, *Proc. SPIE*, **4841**, 1548
- Emsellem, E., Cappellari, M., Krajnović, D., et al. 2007, *MNRAS*, **379**, 401
- Emsellem, E., Cappellari, M., Krajnović, D., et al. 2011, *MNRAS*, **414**, 888
- Emsellem, E., Monnet, G., & Bacon, R. 1994, *A&A*, **285**, 723
- Fahion, K., Lyubenova, M., van de Ven, G., et al. 2019, *A&A*, **628**, A92
- Fahion, K., Lyubenova, M., van de Ven, G., et al. 2021, *A&A*, **650**, A137
- Fahion, K., Müller, O., Rejkuba, M., et al. 2020, *A&A*, **634**, A53
- Falcón-Barroso, J., van de Ven, G., Lyubenova, M., et al. 2019, *A&A*, **632**, A59
- Feldmeier, A., Neumayer, N., Seth, A., et al. 2014, *A&A*, **570**, A2
- Feldmeier-Krause, A., Kerzendorf, W., Do, T., et al. 2020, *MNRAS*, **494**, 396
- Feldmeier-Krause, A., Kerzendorf, W., Neumayer, N., et al. 2017a, *MNRAS*, **464**, 194
- Feldmeier-Krause, A., Neumayer, N., Schödel, R., et al. 2015, *A&A*, **584**, A2
- Feldmeier-Krause, A., Zhu, L., Neumayer, N., et al. 2017b, *MNRAS*, **466**, 4040
- Ferguson, H. C., & Sandage, A. 1989, *ApJL*, **346**, L53
- Ferrarese, L., Côté, P., & Dalla Bontà, E. 2006, *ApJL*, **644**, L21
- Fraternali, F., Cappi, M., Sancisi, R., & Oosterloo, T. 2002a, *ApJ*, **578**, 109
- Fraternali, F., Oosterloo, T., Sancisi, R., & van Moorsel, G. 2001, *ApJL*, **562**, L47
- Fraternali, F., van Moorsel, G., Sancisi, R., & Oosterloo, T. 2002b, *AJ*, **123**, 3124
- Freudling, W., Romaniello, M., Bramich, D. M., et al. 2013, *A&A*, **559**, A96
- Fujita, Y., & Nagashima, M. 1999, *ApJ*, **516**, 619
- García, A. M. 1993, *A&AS*, **100**, 47
- Garnett, D. R., Shields, G. A., Skillman, E. D., Sagan, S. P., & Dufour, R. J. 1997, *ApJ*, **489**, 63
- Gebhardt, K., Lauer, T. R., Kormendy, J., et al. 2001, *AJ*, **122**, 2469
- Gelatt, A. E., Hunter, D. A., & Gallagher, J. S. 2001, *PASP*, **113**, 142
- Georgiev, I. Y., & Böker, T. 2014, *MNRAS*, **441**, 3570
- Georgiev, I. Y., Böker, T., Leigh, N., Lützgendorf, N., & Neumayer, N. 2016, *MNRAS*, **457**, 2122
- Gillessen, S., Plewa, P. M., Eisenhauer, F., et al. 2017, *ApJ*, **837**, 30
- Gonneau, A., Lyubenova, M., Lançon, A., et al. 2020, *A&A*, **634**, A133
- Gordon, K. D., Hanson, M. M., Clayton, G. C., Rieke, G. H., & Misselt, K. A. 1999, *ApJ*, **519**, 165
- Graham, A. W. 2002, *ApJL*, **568**, L13
- Graham, A. W., & Guzmán, R. 2003, *AJ*, **125**, 2936
- Graham, M. T., Cappellari, M., Li, H., et al. 2018, *MNRAS*, **477**, 4711
- Greene, J. E., Leauthaud, A., Emsellem, E., et al. 2018, *ApJ*, **852**, 36
- Grier, C. J., Mathur, S., Ghosh, H., & Ferrarese, L. 2011, *ApJ*, **731**, 60
- Guélin, M., & Weliachew, L. 1969, *A&A*, **1**, 10
- Guérou, A., Emsellem, E., Krajnović, D., et al. 2016, *A&A*, **591**, A143
- Guillard, N., Emsellem, E., & Renaud, F. 2016, *MNRAS*, **461**, 3620
- Harborne, K. E., Power, C., Robotham, A. S. G., Cortese, L., & Taranu, D. S. 2019, *MNRAS*, **483**, 249
- Harborne, K. E., van de Sande, J., Cortese, L., et al. 2020, *MNRAS*, **497**, 2018
- Harris, W. E. 1996, *AJ*, **112**, 1487
- Hartmann, M., Debattista, V. P., Seth, A., Cappellari, M., & Quinn, T. R. 2011, *MNRAS*, **418**, 2697
- Hilker, M., & Richtler, T. 2000, *A&A*, **362**, 895
- Ho, L. C., Filippenko, A. V., & Sargent, W. L. W. 1997, *ApJS*, **112**, 315
- Ho, L. C., Greene, J. E., Filippenko, A. V., & Sargent, W. L. W. 2009, *ApJS*, **183**, 1
- Hoffman, L., Cox, T. J., Dutta, S., & Hernquist, L. 2009, *ApJ*, **705**, 920
- Hunter, D. 1997, *PASP*, **109**, 937
- Hunter, D. A., & Gallagher, J. S. I. 1997, *ApJ*, **475**, 65
- Hunter, D. A., Wilcots, E. M., van Woerden, H., Gallagher, J. S., & Kohle, S. 1998, *ApJL*, **495**, L47
- Ibata, R., Bellazzini, M., Chapman, S. C., et al. 2009, *ApJL*, **699**, L169
- Illingworth, G. 1977, *ApJL*, **218**, L43
- Jarrett, T. H., Chester, T., Cutri, R., Schneider, S. E., & Huchra, J. P. 2003, *AJ*, **125**, 525
- Joseph, C. L., Merritt, D., Olling, R., et al. 2001, *ApJ*, **550**, 668
- Kacharov, N., Neumayer, N., Seth, A. C., et al. 2018, *MNRAS*, **480**, 1973
- Kamann, S., Husser, T. O., Dreizler, S., et al. 2018, *MNRAS*, **473**, 5591
- Kamann, S., Wisotzki, L., & Roth, M. M. 2013, *A&A*, **549**, A71
- Karachentsev, I. D., Dolphin, A. E., Geisler, D., et al. 2002, *A&A*, **383**, 125
- Karachentsev, I. D., Grebel, E. K., Sharina, M. E., et al. 2003, *A&A*, **404**, 93
- Karachentsev, I. D., Makarov, D. I., & Kaisina, E. I. 2013, *AJ*, **145**, 101
- Kennicutt, R. C. J., Lee, J. C., Funes, J. G., et al. 2008, *ApJS*, **178**, 247
- Kormendy, J., & Djorgovski, S. 1989, *ARA&A*, **27**, 235
- Kormendy, J., Drory, N., Bender, R., & Cornell, M. E. 2010, *ApJ*, **723**, 54
- Kormendy, J., & McClure, R. D. 1993, *AJ*, **105**, 1793
- Kraft, R. P., Nolan, L. A., Ponman, T. J., Jones, C., & Raychaudhury, S. 2005, *ApJ*, **625**, 785
- Krajnović, D., Bacon, R., Cappellari, M., et al. 2008, *MNRAS*, **390**, 93
- Kumari, N., James, B. L., & Irwin, M. J. 2017, *MNRAS*, **470**, 4618
- Lagos, C. d. P., Stevens, A. R. H., Bower, R. G., et al. 2018, *MNRAS*, **473**, 4956
- Lahén, N., Naab, T., Johansson, P. H., et al. 2020, *ApJ*, **904**, 71
- Lauer, T. R., Faber, S. M., Ajhar, E. A., Grillmair, C. J., & Scowen, P. A. 1998, *AJ*, **116**, 2263
- Laurikainen, E., Salo, H., Buta, R., Knapen, J. H., & Comerón, S. 2010, *MNRAS*, **405**, 1089
- Licquia, T. C., & Newman, J. A. 2015, *ApJ*, **806**, 96
- Light, E. S., Danielson, R. E., & Schwarzschild, M. 1974, *ApJ*, **194**, 257
- Lim, S., Peng, E. W., Côté, P., et al. 2018, *ApJ*, **862**, 82
- Long, K. S., Charles, P. A., & Dubus, G. 2002, *ApJ*, **569**, 204
- Long, K. S., Dodorico, S., Charles, P. A., & Dopita, M. A. 1981, *ApJL*, **246**, L61
- Lotz, J. M., Telford, R., Ferguson, H. C., et al. 2001, *ApJ*, **552**, 572
- Lyubenova, M., & Tsatsi, A. 2019, *A&A*, **629**, A44
- Lyubenova, M., van den Bosch, R. C. E., Côté, P., et al. 2013, *MNRAS*, **431**, 3364
- Martínez-Delgado, D., Romanowsky, A. J., Gabany, R. J., et al. 2012, *ApJL*, **748**, L24
- Mateo, M. L. 1998, *ARA&A*, **36**, 435
- Mathews, L. D., & Gallagher, J. S. I. 1997, *AJ*, **114**, 1899
- Mayall, N. U., & Aller, L. H. 1942, *ApJ*, **95**, 5
- McConnachie, A. W. 2012, *AJ*, **144**, 4
- McConnachie, A. W., Chapman, S. C., Ibata, R. A., et al. 2006, *ApJL*, **647**, L25
- McConnachie, A. W., Irwin, M. J., Lewis, G. F., et al. 2004, *MNRAS*, **351**, L94
- McConnell, N. J., Ma, C.-P., Murphy, J. D., et al. 2012, *ApJ*, **756**, 179
- McGregor, P. J., Hart, J., Conroy, P. G., et al. 2003, *Proc. SPIE*, **4841**, 1581
- Menéndez-Delmestre, K., Sheth, K., Schinnerer, E., Jarrett, T. H., & Scoville, N. Z. 2007, *ApJ*, **657**, 790
- Merritt, D., Ferrarese, L., & Joseph, C. L. 2001, *Sci*, **293**, 1116
- Mihos, J. C., & Hernquist, L. 1994, *ApJL*, **437**, L47
- Milosavljević, M. 2004, *ApJL*, **605**, L13
- Miner, J., Rose, J. A., & Cecil, G. 2011, *ApJL*, **727**, L15
- Mitzkus, M., Cappellari, M., & Walcher, C. J. 2017, *MNRAS*, **464**, 4789
- Monachesi, A., Trager, S. C., Lauer, T. R., et al. 2012, *ApJ*, **745**, 97
- Monaco, L., Saviane, I., Perina, S., et al. 2009, *A&A*, **502**, L9
- Mostoghiu, R., Di Cintio, A., Knebe, A., et al. 2018, *MNRAS*, **480**, 4455
- Mould, J., Kristian, J., & Da Costa, G. S. 1984, *ApJ*, **278**, 575
- Mucciarelli, A., Bellazzini, M., Ibata, R., et al. 2017, *A&A*, **605**, A46
- Neumayer, N., Cappellari, M., Reunanen, J., et al. 2007, *ApJ*, **671**, 1329
- Neumayer, N., Seth, A., & Böker, T. 2020, *A&ARv*, **28**, 4
- Nguyen, D. D., Seth, A. C., den Brok, M., et al. 2017, *ApJ*, **836**, 237
- Nguyen, D. D., Seth, A. C., Neumayer, N., et al. 2018, *ApJ*, **858**, 118
- Nguyen, D. D., Seth, A. C., Neumayer, N., et al. 2019, *ApJ*, **872**, 104
- Noyola, E., Gebhardt, K., & Bergmann, M. 2008, *ApJ*, **676**, 1008
- Oh, K. S., & Lin, D. N. C. 2000, *ApJ*, **543**, 620
- Olling, R. P. 1996, *AJ*, **112**, 457
- Paudel, S., Lisker, T., & Kuntschner, H. 2011, *MNRAS*, **413**, 1764
- Peçetti, R., Seth, A., Neumayer, N., et al. 2020, *ApJ*, **900**, 32
- Perets, H. B., & Mastrobuono-Battisti, A. 2014, *ApJL*, **784**, L44
- Pfeffer, J., & Baumgardt, H. 2013, *MNRAS*, **433**, 1997
- Pfeffer, J., Lardo, C., Bastian, N., Saracino, S., & Kamann, S. 2021, *MNRAS*, **500**, 2514

- Pfeffer, J. L., Trujillo-Gomez, S., Kruijssen, J. M. D., et al. 2020, *MNRAS*, **499**, 4863
- Pinna, F., Falcón-Barroso, J., Martig, M., et al. 2019, *A&A*, **623**, A19
- Portegies Zwart, S. F., McMillan, S. L. W., & Gieles, M. 2010, *ARA&A*, **48**, 431
- Putman, M. E., Peek, J. E. G., Muratov, A., et al. 2009, *ApJ*, **703**, 1486
- Radburn-Smith, D. J., Roškar, R., Debattista, V. P., et al. 2012, *ApJ*, **753**, 138
- Redman, R. O., & Shirley, E. G. 1937, *MNRAS*, **97**, 416
- Robles-Valdez, F., Carigi, L., & Peimbert, M. 2013, *MNRAS*, **429**, 2351
- Rose, J. A., Arimoto, N., Caldwell, N., et al. 2005, *AJ*, **129**, 712
- Rossa, J., van der Marel, R. P., Böker, T., et al. 2006, *AJ*, **132**, 1074
- Sacchi, E., Cignoni, M., Aloisi, A., et al. 2019, *ApJ*, **878**, 1
- Sánchez-Janssen, R., Côté, P., Ferrarese, L., et al. 2019, *ApJ*, **878**, 18
- Schiavon, R. P., Caldwell, N., & Rose, J. A. 2004, *AJ*, **127**, 1513
- Schinnerer, E., Böker, T., Emsellem, E., & Lisenfeld, U. 2006, *ApJ*, **649**, 181
- Schinnerer, E., Böker, T., & Meier, D. S. 2003, *ApJL*, **591**, L115
- Schödel, R., Feldmeier, A., Kunneriath, D., et al. 2014, *A&A*, **566**, A47
- Semczuk, M., Łokas, E. L., Salomon, J.-B., Athanassoula, E., & D’Onghia, E. 2018, *ApJ*, **864**, 34
- Seth, A., de Jong, R., Dalcanton, J., & GHOSTS Team 2007, IAU Symp. 241, Stellar Populations as Building Blocks of Galaxies, ed. A. Vazdekis & R. F. Peletier (Cambridge: Cambridge Univ. Press), 523
- Seth, A. C. 2010, *ApJ*, **725**, 670
- Seth, A. C., Blum, R. D., Bastian, N., Caldwell, N., & Debattista, V. P. 2008, *ApJ*, **687**, 997
- Seth, A. C., Cappellari, M., Neumayer, N., et al. 2010, *ApJ*, **714**, 713
- Seth, A. C., Dalcanton, J. J., & de Jong, R. S. 2005a, *AJ*, **129**, 1331
- Seth, A. C., Dalcanton, J. J., & de Jong, R. S. 2005b, *AJ*, **130**, 1574
- Seth, A. C., Dalcanton, J. J., Hodge, P. W., & Debattista, V. P. 2006, *AJ*, **132**, 2539
- Seth, A. C., van den Bosch, R., Mieske, S., et al. 2014, *Natur*, **513**, 398
- Shapley, H. 1943, *Galax* (Philadelphia: Blakiston), 50
- Sheth, K., Regan, M., Hinz, J. L., et al. 2010, *PASP*, **122**, 1397
- Shields, J. C., & Filippenko, A. V. 1992, in ASP Conf. Ser. 31, Relationships Between Active Galactic Nuclei and Starburst Galaxies, ed. A. V. Filippenko (San Francisco, CA: ASP), 267
- Shostak, G. S. 1973, *A&A*, **24**, 411
- Silge, J. D., & Gebhardt, K. 2003, *AJ*, **125**, 2809
- Silk, J., Wyse, R. F. G., & Shields, G. A. 1987, *ApJL*, **322**, L59
- Simien, F., & Prugniel, P. 2002, *A&A*, **384**, 371
- Smith, G., Elmegreen, B. G., & Elmegreen, D. M. 1984, *MNRAS*, **210**, 399
- Spekkens, K., & Sellwood, J. A. 2007, *ApJ*, **664**, 204
- Spengler, C., Côté, P., Roediger, J., et al. 2017, *ApJ*, **849**, 55
- Tacconi, L. J., van der Hulst, J. M., & Wesselius, P. R. 1990, NASA Conference Publication, Vol. 3084, ed. D. J. Hollenbach, J. Thronson, & A. Harley (Washington, DC: NASA), 279
- Tachihara, K., Gratier, P., Sano, H., et al. 2018, *PASJ*, **70**, S52
- Theis, C., & Kohle, S. 2001, *A&A*, **370**, 365
- Thilker, D. A., Bianchi, L., Schiminovich, D., et al. 2010, *ApJL*, **714**, L171
- Thilker, D. A., Braun, R., Waltherbos, R. A. M., et al. 2004, *ApJL*, **601**, L39
- Tikhonov, N. A., Galazutdinova, O. A., & Aparicio, A. 2003, *A&A*, **401**, 863
- Tody, D. 1986, Proc. SPIE, **627**, 733
- Tody, D. 1993, in ASP Conf. Ser. 52, Astronomical Data Analysis Software and Systems II, ed. R. J. Hanisch, R. J. V. Brissenden, & J. Barnes (San Francisco, CA: ASP), 173
- Tremaine, S. D., Ostriker, J. P., & Spitzer, L. 1975, *ApJ*, **196**, 407
- Trujillo, I., Aguerri, J. A. L., Cepa, J., & Gutiérrez, C. M. 2001, *MNRAS*, **328**, 977
- Tsatsi, A., Mastrobuono-Battisti, A., van de Ven, G., et al. 2017, *MNRAS*, **464**, 3720
- Valdez-Gutiérrez, M., Rosado, M., Puerari, I., et al. 2002, *AJ*, **124**, 3157
- Valenzuela, O., Hernandez-Toledo, H., Cano, M., et al. 2014, *AJ*, **147**, 27
- Valluri, M., Ferrarese, L., Merritt, D., & Joseph, C. L. 2005, *ApJ*, **628**, 137
- van de Sande, J., Bland-Hawthorn, J., Brough, S., et al. 2017b, *MNRAS*, **472**, 1272
- van de Sande, J., Bland-Hawthorn, J., Fogarty, L. M. R., et al. 2017a, *ApJ*, **835**, 104
- van den Bergh, S. 1995, *AJ*, **110**, 613
- van den Bosch, R. C. E., & de Zeeuw, P. T. 2010, *MNRAS*, **401**, 1770
- van der Marel, R. P., & Franx, M. 1993, *ApJ*, **407**, 525
- van der Marel, R. P., & Guhathakurta, P. 2008, *ApJ*, **678**, 187
- van Woerden, H., van Driel, W., Braun, R., & Rots, A. H. 1993, *A&A*, **269**, 15
- Verolme, E. K., Cappellari, M., Copin, Y., et al. 2002, *MNRAS*, **335**, 517
- Voggel, K. T., Seth, A. C., Neumayer, N., et al. 2018, *ApJ*, **858**, 20
- Walcher, C. J., Böker, T., Charlot, S., et al. 2006, *ApJ*, **649**, 692
- Walcher, C. J., van der Marel, R. P., McLaughlin, D., et al. 2005, *ApJ*, **618**, 237
- Wallace, L., & Hinkle, K. 1996, *ApJS*, **107**, 312
- Walo-Martín, D., Falcón-Barroso, J., Dalla Vecchia, C., Pérez, I., & Negri, A. 2020, *MNRAS*, **494**, 5652
- White, R. L., Long, K. S., Becker, R. H., et al. 2019, *ApJS*, **241**, 37
- Whitmore, B. C., Chandar, R., Lee, J., et al. 2020, *ApJ*, **889**, 154
- Wiklund, T., & Henkel, C. 1990, *A&A*, **227**, 394
- Williams, B. F., Dalcanton, J. J., Gilbert, K. M., et al. 2010a, *ApJ*, **716**, 71
- Williams, B. F., Dalcanton, J. J., Stilp, A., et al. 2010b, *ApJ*, **709**, 135
- Williams, B. F., Dalcanton, J. J., Stilp, A., et al. 2013, *ApJ*, **765**, 120
- Young, L. M., & Lo, K. Y. 1997, *ApJ*, **476**, 127
- Yukita, M., Swartz, D. A., Soria, R., & Tennant, A. F. 2007, *ApJ*, **664**, 277
- Zheng, Y., Peek, J. E. G., Werk, J. K., & Putman, M. E. 2017, *ApJ*, **834**, 179
- Zinnecker, H., & Cannon, R. D. 1986, Star Forming Dwarf Galaxies and Related Objects. Proceedings of a workshop held at Paris, France, 1–3 July 1985, ed. D. Kunth, T. X. Thuan, & J. Tran Thanh Van (Gif-sur-Yvette: Éditions Frontières), 155
- Zschaechner, L. K., Rand, R. J., Heald, G. H., Gentile, G., & Kamphuis, P. 2011, *ApJ*, **740**, 35